Geophysical Journal International

Geophys. J. Int. (2016) **204,** 1579–1600
GJI Geodynamics and tectonics

doi: 10.1093/gji/ggv539

The crustal structure of Ellesmere Island, Arctic Canada—teleseismic mapping across a remote intraplate orogenic belt

Christian Schiffer,[1] Randell Stephenson,[1,2] Gordon N. Oakey[3] and Bo H. Jacobsen[1]

[1] *Department of Geoscience, Aarhus University,* 8000 *Aarhus, Denmark. E-mail: christian.schiffer@geo.au.dk*
[2] *School of Geosciences, University of Aberdeen, Aberdeen AB*24 3*UE, United Kingdom*
[3] *Geological Survey of Canada,* 1 *Challenger Drive, Dartmouth NS B*2*Y* 4*A*2, *Canada*

Accepted 2015 December 14. Received 2015 December 14; in original form 2015 September 22

SUMMARY

Ellesmere Island in Arctic Canada displays a complex geological evolution. The region was affected by two distinct orogenies, the Palaeozoic Ellesmerian orogeny (the Caledonian equivalent in Arctic Canada and Northern Greenland) and the Palaeogene Eurekan orogeny, related to the opening of Baffin Bay and the consequent convergence of the Greenland plate. The details of this complex evolution and the present-day deep structure are poorly constrained in this remote area and deep geophysical data are sparse. Receiver function analysis of seven temporary broad-band seismometers of the Ellesmere Island Lithosphere Experiment complemented by two permanent stations provides important data on the crustal velocity structure of Ellesmere Island. The crustal expression of the northernmost tectonic block of Ellesmere Island (∼82°–83°N), Pearya, which was accreted during the Ellesmerian orogeny, is similar to that at the southernmost part, which is part of the Precambrian Laurentian (North America-Greenland) craton. Both segments have thick crystalline crust (∼35–36 km) and comparable velocity–depth profiles. In contrast, crustal thickness in central Ellesmere Island decreases from ∼24–30 km in the Eurekan fold and thrust belt (∼79.7°–80.6°N) to ∼16–20 km in the Hazen Stable Block (HSB; ∼80.6°–81.4°N) and is covered by a thick succession of metasediments. A deep crustal root (∼48 km) at ∼79.6°N is interpreted as cratonic crust flexed beneath the Eurekan fold and thrust belt. The Carboniferous to Palaeogene sedimentary succession of the Sverdrup Basin is inferred to be up to 1–4 km thick, comparable to geologically-based estimates, near the western margin of the HSB.

Key words: Body waves; Intra-plate processes; Continental tectonics: compressional; Crustal structure; Arctic region.

1 INTRODUCTION

Ellesmere Island is situated in Nunavut, Arctic Canada, and is part of the Canadian Arctic Archipelago, extending from Baffin Bay at ∼76°–78°N to the passive continental margin of the Arctic Ocean in the north at ∼81°–83°N. The narrow SSW–NNE oriented Nares Strait forms its eastern boundary with Greenland at ∼60°–75°W and Nansen Sound its western boundary with Axel Heiberg Island at ∼90°W (Fig. 1). Most geological features, especially in the central and northern parts of Ellesmere Island, including topography, faults and structural units generally display a SW–NE trend. The major topographic elements include the Grantland Uplift (up to ∼1800 m), the Victoria and Albert Mountains in the north (up to ∼1900 m), the Hazen Trough in between these with substantially lower topography (∼250–800 m) and the Inglefield Uplift (∼1700 m) in the Canadian Shield in the south (Fig. 1). The Axel Heiberg Mountains (∼1600 m) form a topographic high on Axel Heiberg Island in the deformed Sverdrup Basin just west of Ellesmere Island (Fig. 1). The Sverdrup Basin, in many places affected by deformation and/or salt diapirism, covers mainly the western part of Ellesmere Island (Embry 1991) (Fig. 1, stippled white outline).

Ellesmere Island experienced two major orogenic events. During the Palaeozoic Ellesmerian orogeny (the Arctic Canada-Greenland equivalent of the Caledonian orogeny) different terranes and blocks accreted at the Franklinian passive continental margin of Laurentia (Gasser 2013; Gee 2015). The Eocene intraplate Eurekan orogeny was caused by relative motions between Greenland and Canada responding to plate boundary reconfigurations in Baffin Bay and the North Atlantic and Arctic Ocean basins (Tessensohn & Piepjohn 2000; Nielsen *et al.* 2007; Oakey & Chalmers 2012).

Geophysical data are sparse in the study area. Deep seismic reflection and wide angle refraction data (shown on Fig. 2) are limited to the marine areas surrounding Ellesmere Island, such as Nares Strait and northern Baffin Bay (Jackson & Reid 1994; Reid & Jackson 1997; Funck *et al.* 2006; Neben *et al.* 2006; Reid *et al.* 2006;

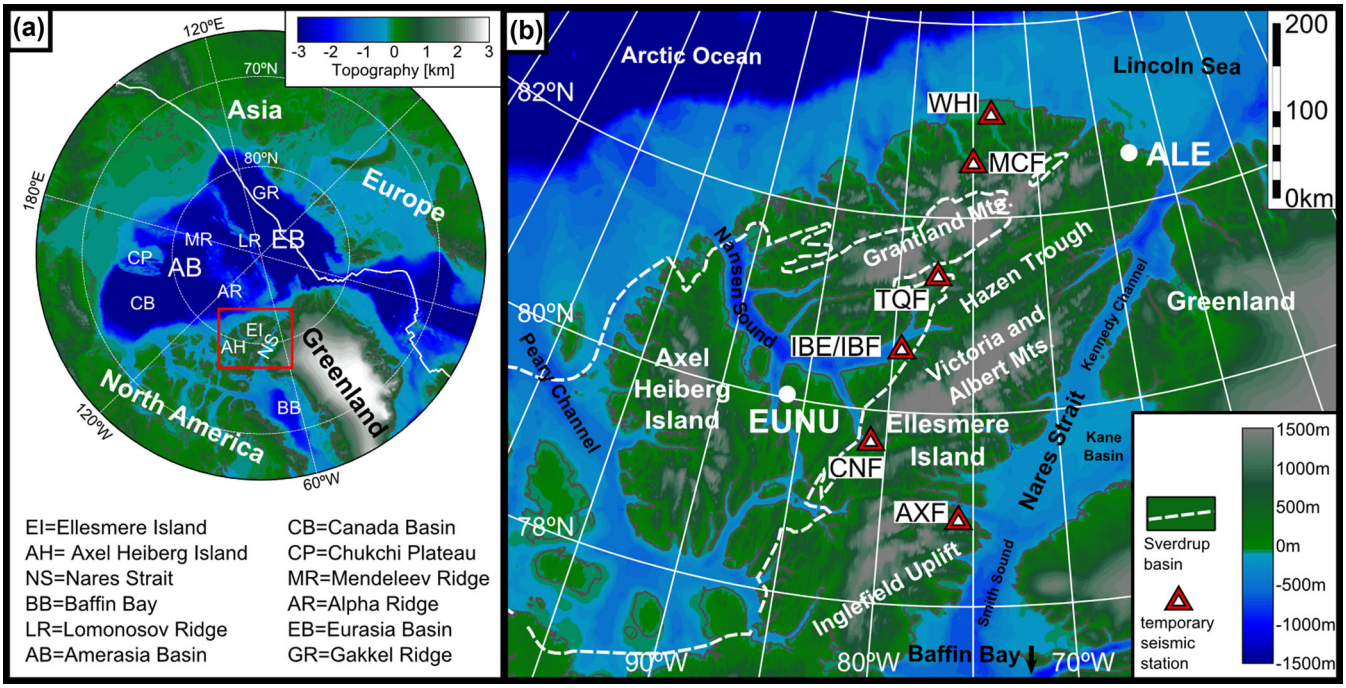

Figure 1. Study area. (a) Circum Arctic overview with topography. Red box marks the study area. (b) Overview map of the study area showing topography (ETOPO1; Amante & Eakins 2009), the ELLITE temporary station positions (red triangles; see Table 1), the outline of Sverdrup Basin sedimentary cover (white stippled line; Oakey & Stephenson 2008), the locations of Eureka (EUNU) and Alert (ALE) seismic stations and geographical names (Trettin 1991).

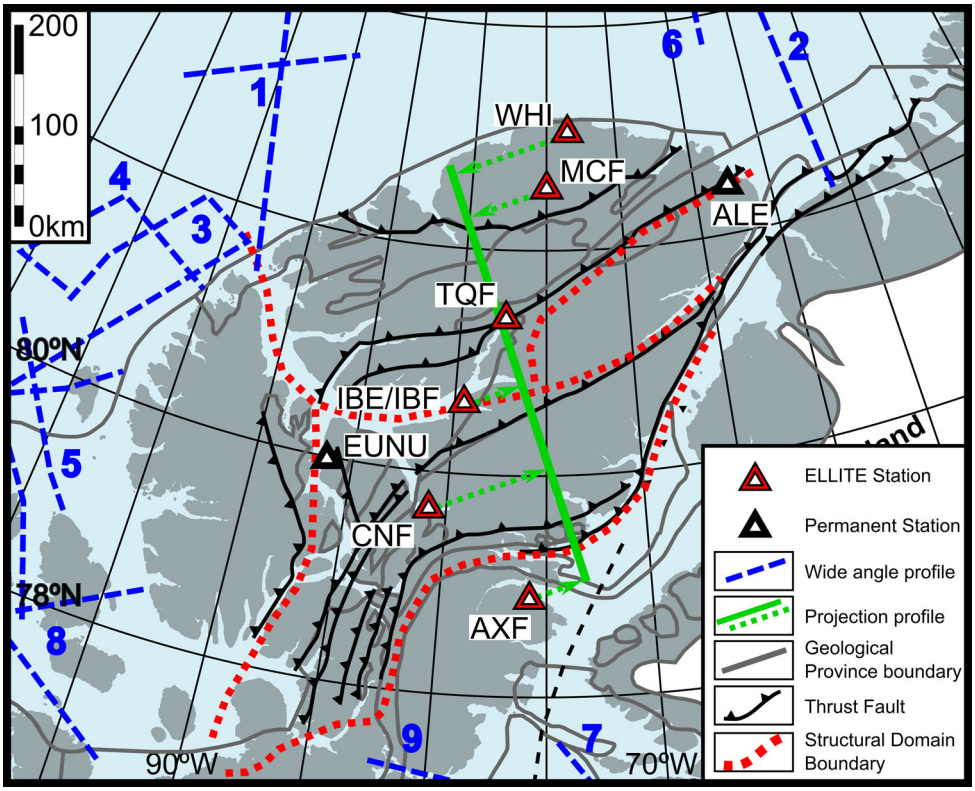

Figure 2. Overview map of the study area showing the broad-band seismic stations (red triangles: ELLITE temporary stations; black triangles: permanent stations), wide angle seismic profiles (blue dashed lines) and the projection profile defined for the RF analysis (green) in the context of major faults and structural boundaries (black lines and red dotted lines, respectively; see Fig. 3). References for the wide-angle data: 1: Funck *et al.* (2011); 2: Jackson & Dahl-Jensen (2010); 3–5: Argyle & Forsyth (1994); 6: Forsyth *et al.* (1994); 7: Reid & Jackson (1997); 8: Forsyth *et al.* (1979); 9: Funck *et al.* (2006).

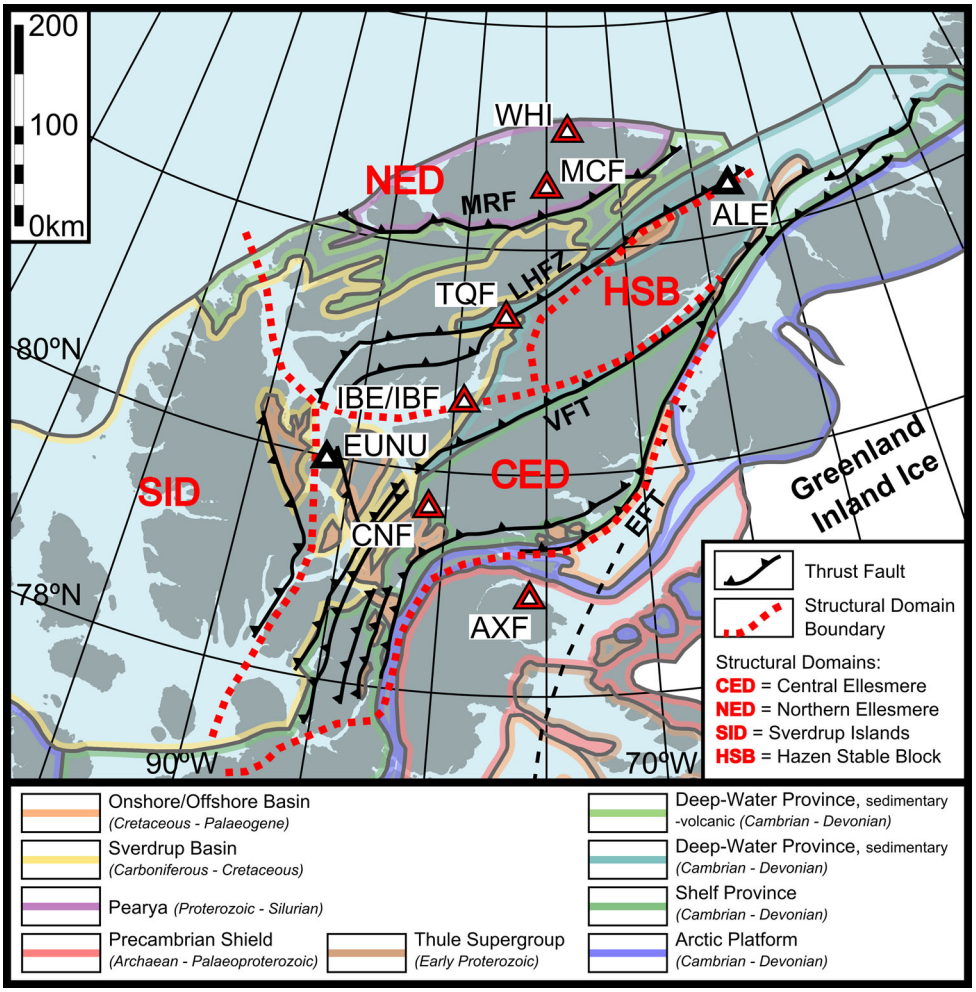

Figure 3. Geological map of the study area (modified after Oakey & Stephenson 2008). Eurekan 'Structural Domains' are from Okulitch & Trettin (1991). Faults: MRF—Mount Rawlinson Fault; LHFZ—Lake Hazen Fault Zone; VFT—Vesle Fiord Thrust; EFT—Eurekan Frontal Thrust. Black triangles: permanent stations. Red triangles: ELLITE stations (see Table 1).

Tessensohn *et al.* 2006) as well as the eastern Sverdrup Basin and the Arctic passive margin (Forsyth *et al.* 1979; Sobczak *et al.* 1986; Sweeney *et al.* 1986; Asudeh *et al.* 1989; Argyle *et al.* 1992; Forsyth *et al.* 1994; Forsyth *et al.* 1998; Jackson & Dahl-Jensen 2010; Funck *et al.* 2011). These are complemented by area-wide aeromagnetic (Coles 1985; Haines 1985; Kovacs *et al.* 1986; Okulitch *et al.* 1990; Oakey & Damaske 2006; Matzka 2010) and gravity data (Stephenson & Ricketts 1989; Stephenson & Ricketts 1990; Oakey *et al.* 2001; Oakey & Stephenson 2008) allowing for large-scale interpretations of Arctic provinces (Alvey *et al.* 2008; Gaina *et al.* 2011; Saltus *et al.* 2011; Pease *et al.* 2014).

Passive seismological data are almost absent in this area: only two permanent seismic observatories at Eureka and Alert (Fig. 1), which have been used for receiver function (RF; Darbyshire 2003) and surface wave studies (Darbyshire 2005) are available.

The Ellesmere Island Lithosphere Experiment (ELLITE; Stephenson *et al.* 2013) was carried out to address the absence of crustal structure constraints in this region of complex geology and tectonics. The ELLITE array included seven broad-band seismometers at six geographical locations (Fig. 2), which were deployed and maintained for a period of 2 yr (2010–2012), supplemented by the permanent stations at Eureka (EUNU) and Alert (ALE). Teleseismic waveforms were analysed with the RF method, which is able to image velocity discontinuities (such as the Moho) beneath the receiving seismometer. The ELLITE array has provided, for the first time, seismically constrained information of the large-scale crustal structure of Ellesmere Island.

2 TECTONIC FRAMEWORK AND GEOLOGY ALONG THE ELLITE ARRAY

The topographic and crustal expression of Ellesmere Island was shaped by two orogenic events with intervening periods of extensional tectonics, the main expression of which is the Sverdrup Basin.

The Palaeozoic Ellesmerian Orogeny involved the accretion of an assemblage of deep water basins, arcs, continental fragments and exotic microcontinents to the older Franklinian passive margin of the Laurentian palaeocontinent (Trettin 1987; Beranek *et al.* 2010; Lemieux *et al.* 2011; Anfinson *et al.* 2012a,b; Hadlari *et al.* 2014; Beranek *et al.* 2015) and is the equivalent or prolongation of the Caledonian orogeny in the North Atlantic (Gee 2015). Pearya, the northernmost part of Ellesmere Island (Fig. 3) represents such an exotic microcontinent, accreted in the late Silurian (Trettin 1987). The suture between autochthonous Laurentia (exposed on southern Ellesmere Island and Greenland, *cf.* Fig. 3) and Ellesmerian accreted terranes is

inferred to lie within the Hazen Stable Block (HSB; Fig. 3), the bedrock of which mainly comprises Late Precambrian–Early Palaeozoic deep water sedimentary rocks with strong Ellesmerian deformation. The Franklinian passive margin succession is exposed to the south of the HSB, comprising slope, then shelf and finally platform facies sediments overlying Laurentian crystalline basement and displaying progressively less Ellesmerian deformation.

The Sverdrup Basin subsided from the Permian until the Palaeogene, attributed to extensional collapse of the Ellesmerian Orogen and subsequent thermal relaxation (Stephenson *et al.* 1987; Embry 1991). It covers an area of about 1300 km length (in southwest–northeast direction, beyond the border of Fig. 3) and 400 km width with over 2 km of Palaeozoic strata (Davies & Nassichuk 1991) and between 9 and 13 km of Mesozoic–Palaeogene sediments (Embry 1991; Embry & Beauchamp 2008). The margin of the Sverdrup Basin on Ellesmere Island is depositional in places, including fault-bounded, and erosional in others (e.g. Ricketts & Stephenson 1994).

Most magmatism in the study area is of Cretaceous age (Embry & Osadetz 1988; Davies & Nassichuk 1991; Estrada & Henjes-Kunst 2004; Tegner *et al.* 2011) and linked with the High Arctic Large Igneous Province (HALIP), which is mainly expressed offshore as the Alpha-Mendeleev Ridge complex in the Amerasia segment of the Arctic Ocean (Døssing *et al.* 2013b; Pease *et al.* 2014). Magmatic rocks of any significance are not a major feature of the geology around any of the ELLITE stations.

The Arctic Canada realm became dominated by extensional tectonics during the period in which the Sverdrup Basin was subsiding passively in the Mesozoic. Around the same time as the emplacement of the HALIP, and likely related to it, rifting and continental breakup led to the formation of the present Canadian polar continental margin of the Arctic Ocean (Døssing *et al.* 2013a,b). Partly contemporaneous to this, the Labrador Sea and Baffin Bay opened from south to north between Greenland and Canada during the latest Cretaceous and Palaeogene (Srivastava 1985; Roest & Srivastava 1989; Oakey & Chalmers 2012; Hosseinpour *et al.* 2013).

The formation of the Labrador Sea and Baffin Bay led directly to a compressional phase, and also the final major tectonic event affecting the study area. The Palaeogene Eurekan Orogeny formed in an intraplate setting, not involving the closure of an ocean or accretion of exotic terranes. Compression and shortening across Ellesmere Island and adjacent regions in Canada and Greenland culminated in the Eocene as a result of sea floor spreading in Labrador Sea-Baffin Bay and associated plate boundary reconfigurations in the incipient North Atlantic–Arctic Eurasian Basin realm (Tessensohn & Piepjohn 2000; Nielsen *et al.* 2007; Oakey & Chalmers 2012). Among the most significant, evidence for Eurekan deformation is displayed north and west of the Eurekan Frontal Thrust (EFT; Fig. 3) where the Central Ellesmerian Fold and Thrust Belt, within the Central Ellesmere Domain (CED; Fig. 3), accommodated up to 100 km of additional Eurekan crustal shortening (Harrison & de Freitas 2007). Ellesmerian structures on Ellesmere Island were also reactivated during Eurekan orogenesis, particularly in the Northern Ellesmere Domain (NED; Fig. 3) but much less so in the HSB and CED (Grist & Zentilli 2006; Tessensohn *et al.* 2006; Piepjohn *et al.* 2008; Tessensohn *et al.* 2012). The former (HSB) is bounded north and south by the Hazen Lake Fault Zone and the Vesle Fiord Thrust, respectively (Fig. 3; HLFZ and VFT), both of which are predominantly Eurekan-aged structures. Eurekan-aged structures are also observed in the Sverdrup Island Domain (SID; Fig. 3) as E- and NE-vergent thrusts with associated folds, faults and salt diapirism in the Sverdrup Basin (Okulitch & Trettin 1991; Harrison 2006), including what has been interpreted as crustal or lithospheric buckling (Stephenson & Ricketts 1990; Stephenson *et al.* 1990). Døssing *et al.* (2014) interpreted compressional structures as far north as the Licoln Sea margin and the Lomonossov Ridge to be products of Eurekan shortening.

The ELLITE transect crosses all of these tectonic terranes and the local geological setting for each station can be summarised as follows. Station WHI and station MCF are both within Pearya. The suture between Pearya and the Franklinian margin is represented by the Mount Rawlinson Fault (Fig. 3), nearby station MCF. Station TQF and station ALE are both close to the Lake Hazen Fault Zone (LHFZ; Fig. 3), an Ellesmerian structure strongly reactivated during the Eurekan, on which crustal units of the NED are thrust over the HSB. Station TQF is near the margin of the present-day extent of Sverdrup Basin strata. Stations IBE and IBF lie within the HSB, which comprises Early Palaeozoic strata severely deformed during the Ellesmerian Orogeny overlain by essentially undeformed Sverdrup Basin strata that are nevertheless older than the Eurekan Orogeny. Station EUNU lies in a similar setting, SW along strike of the HSB where Sverdrup Basin strata are thicker and Eurekan-aged structures are dominant and become geometrically more complex (SID; Fig. 3). Station CNF lies within the CED, dominated by the primarily Eurekan-aged Central Ellesmere Fold and Thrust Belt, which consists of Neoproterozoic and Early Palaeozoic strata of the Franklinian passive continental margin succession. Station AXF lies on cratonic basement near the edge of the Cambrian-Devonian strata of the Arctic platform, landward of the contemporaneous Franklinian passive continental margin sedimentary succession.

3 FIELD PROGRAMME AND DATA ACQUISITION

ELLITE was a seismological experiment on Ellesmere Island, consisting of an array of 7 three-component broad-band seismometers at six locations and spanning approximately 450 km from the Arctic Ocean (83°N) to the western Kane Basin (79°N). The array was deployed for a period of 2+ yr from 2010 June through 2012 August, including a maintenance visit in 2011, which excluded one station (AXF). Instruments of two types (Guralp 3Ts and Guralp 3ESPDs) were deployed and equipped with solar panels to provide a continuous power supply, except of during the winter darkness. The instruments and equipment were provided by SEIS-UK. The only two permanent stations in this region, at Eureka (EUNU) and Alert (ALE), ∼50 km west and ∼100 km east of the array, respectively, are included in this study. Station information, including locations, instrumentation and technical details, is listed in Table 1. Two observatories of different instrumentation were deployed at the same location (IBE and IBF). Consult Stephenson *et al.* (2013) for further details.

The data are generally of high quality. All stations show ‘shut down’ gaps during the winter seasons because of a lack of solar power for charging batteries. Some instrument malfunctions occurred at some of the stations, which partly limited the recording time and thereby the useable earthquake signals. Station AXF did not collect data after 2011 April because of animal damage and could not be repaired during the maintenance visit due to ground conditions preventing the service aircraft from landing. WHI and MCF did not restart after winter shut down 2010–2011 and therefore did not record data. While WHI was repaired and recorded regularly during the remaining period, MCF did not collect any further data because of instrument malfunction despite servicing in 2011. For the same reason, station IBE did not record any data after

Table 1. Station overview and information.

Station name	Location	Latitude (N)	Longitude (W)	Elevation	Instrument	Recording period	Number of mass adjustments
AXF	Alexandra Fiord	78.88	75.78	30	Guralp 3T	2010 June–2011 March	486
CNF	Canyon Fiord	79.66	80.78	43	Guralp ESPD	2010 June–2012 August	169
EUNU	Eureka	80.05	86.42	628		2000–present	–
IBE (*IBF-E*)	D'Iberville Fiord	80.61	79.58	34	Guralp ESPD	2010 June–2011 October	380
IBF (*IBF-B*)	D'Iberville Fiord	80.61	79.58	34	Guralp 3T	2010 June–2012 August	4882
TQF	Tanquary Fiord	81.41	76.85	20	Guralp ESPD	2010 June–2012 August	no information
ALE	Alert	82.50	62.35			1991–present	–
MCF	M'Clintock Inlet	82.65	75.04	99	Guralp ESPD	2010 June–2011 November	45
WHI	Ward Hunt Island	83.99	74.15	44	Guralp 3T	2010 June–2012 August	29

Table 2. Recording times of ELLITE stations.

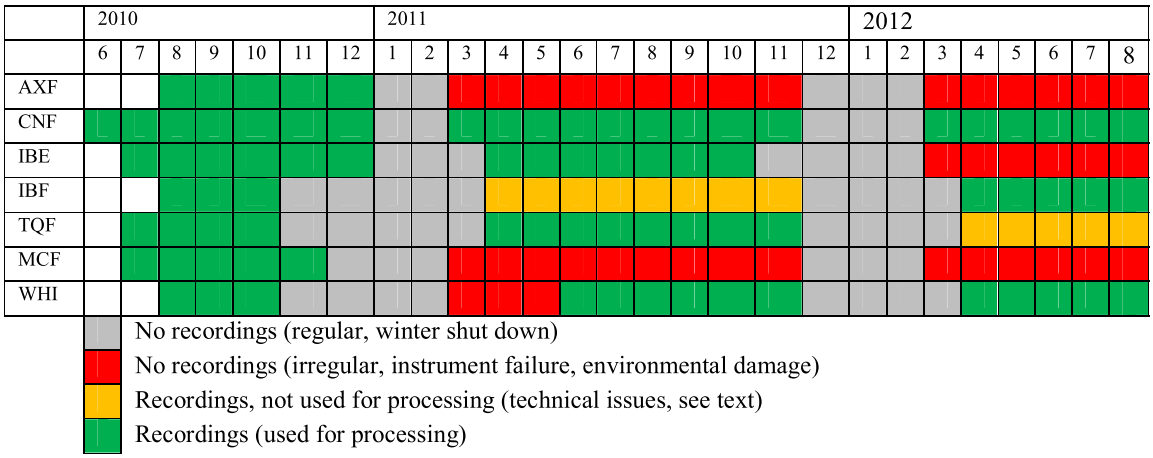

winter 2011/2012. All other stations recorded regularly during the entire time of deployment from 2010 June through 2012 August, excluding winter shut down gaps.

Besides the data loss periods described above, two stations encountered technical issues while recording. TQF shows waveforms but no distinct first arrivals of seismic events in 2012. Whether this was due to damage or a timing error could not be determined. IBF showed unreasonably high amplitudes on the vertical component compared to the horizontal components in 2011, resulting in errors during processing. Therefore, data from this season were disregarded. The instrument's log files indicate frequent attempts to adjust the internal masses (4882 attempts in 2 yr), which was almost entirely limited to the season of 2011 (4864). In contrast, the same instrument type at WHI only made 29 mass adjustments over two years. A tilt or a technical problem of the masses after winter 2010/2011 could change the effective angle of the incident wave relative to the instrument and would cause distortion of the recorded data.

Table 2 summarizes the recording status of all ELLITE stations during the entire experiment, including data gaps, technical issues and periods of good data recordings. At one of the temporary stations (CNF), the maximum possible amount of data was recorded and at another (WHI), only three months are missing while at two other stations (IBF, TQF) one season showed defective waveforms, which were disregarded in the data processing.

The majority of the recorded earthquakes originate from the Pacific convergent plate boundaries, especially close to Japan, which results in a clear peak of events from the northwest (backazimuths ∼270°–360°) with regard to the station positions (Fig. 4 and Fig. A1). The teleseismic events of magnitude larger than 4.5 (6.3 for the permanent stations) are used in further processing. The details of the processing are explained in the following sections.

4 RECEIVER FUNCTIONS

P-to-*S* RFs were estimated from the waveforms recorded from the three-component seismometers of the ELLITE array (Section 4.1). To extract more spatial variation of the geological structure in the subsurface around the station bins were created in different azimuthal directions (Section 4.2). Estimates of the apparent shear wave velocity variation with signal period ($V_{S\mathrm{app}}$), derived from the RF waveforms, were employed as an additional constraint of the absolute *S*-wave velocities at each station (Section 4.3). Both RFs and $V_{S\mathrm{app}}$ were finally utilised in an inverse approach to obtain absolute velocity models of the subsurface at each station (Section 5). The details of this procedure are described in the following sections. The general procedure was based on the approach presented in Schiffer *et al.* (2015). The differences in this study compared to Schiffer *et al.* (2015) are: (i) an additional modelling step was included, parametrising the initial coarse velocity models into many thin layers; (ii) the available data were subdivided into different azimuthal bins at most stations and (iii) inversion was carried out with different parametrisations of the same data.

4.1 *P*-to-*S* receiver function estimation

P-to-*S* RFs isolate conversions of teleseismic *P* waves to *S* waves at velocity discontinuities recorded on three-component waveforms (Langston 1979; Ammon 1991; Kind *et al.* 1995; Bostock 1998). The waveforms of the recorded horizontal N- and E-components

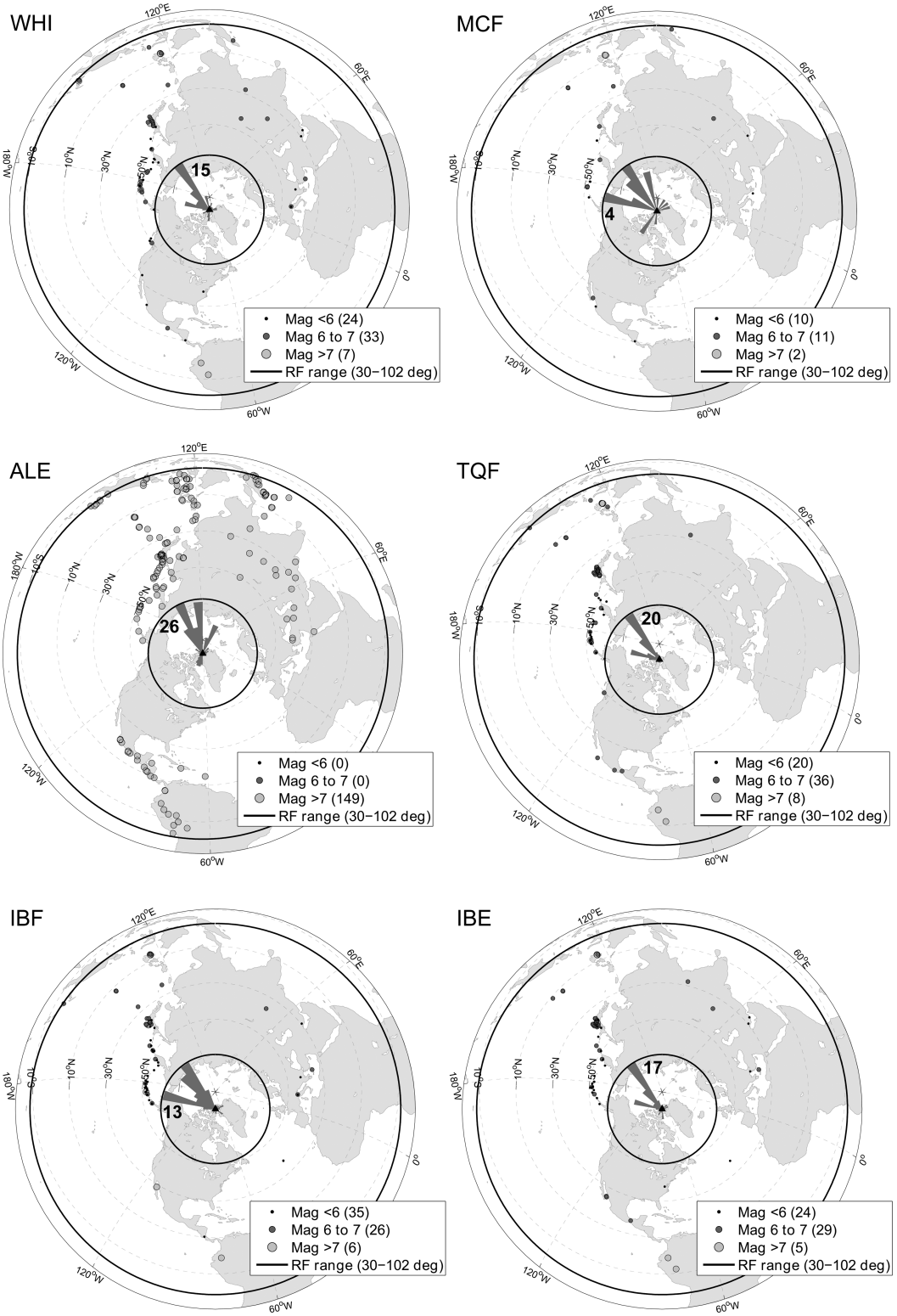

Figure 4. Epicentral plots showing the earthquake locations of all events used for the receiver function processing. The earthquakes are grouped with regard to magnitude (Mag < 6, $6 <$ Mag < 7, Mag > 7). A histogram of the backazimuth (BAZ) of the events to the station is shown in the centre. The centre indicates zero events, the number inside the inner black circle indicates the maximum number with a linear scale along the radius.

(north and east) were initially rotated into the direction of the incident earthquake wave, which creates the R- and T-components (radial and transversal) in addition to the original Z-component (vertical). Further vertical rotation on the R–Z plane into the direction of the incidence angle was applied, which creates the theoretical L- and Q-components, respectively (Vinnik 1977). Both R- and Q-RFs were produced and further analysed, with the difference that R-RFs show a fraction of the incoming *P*-wave signal, whereas this

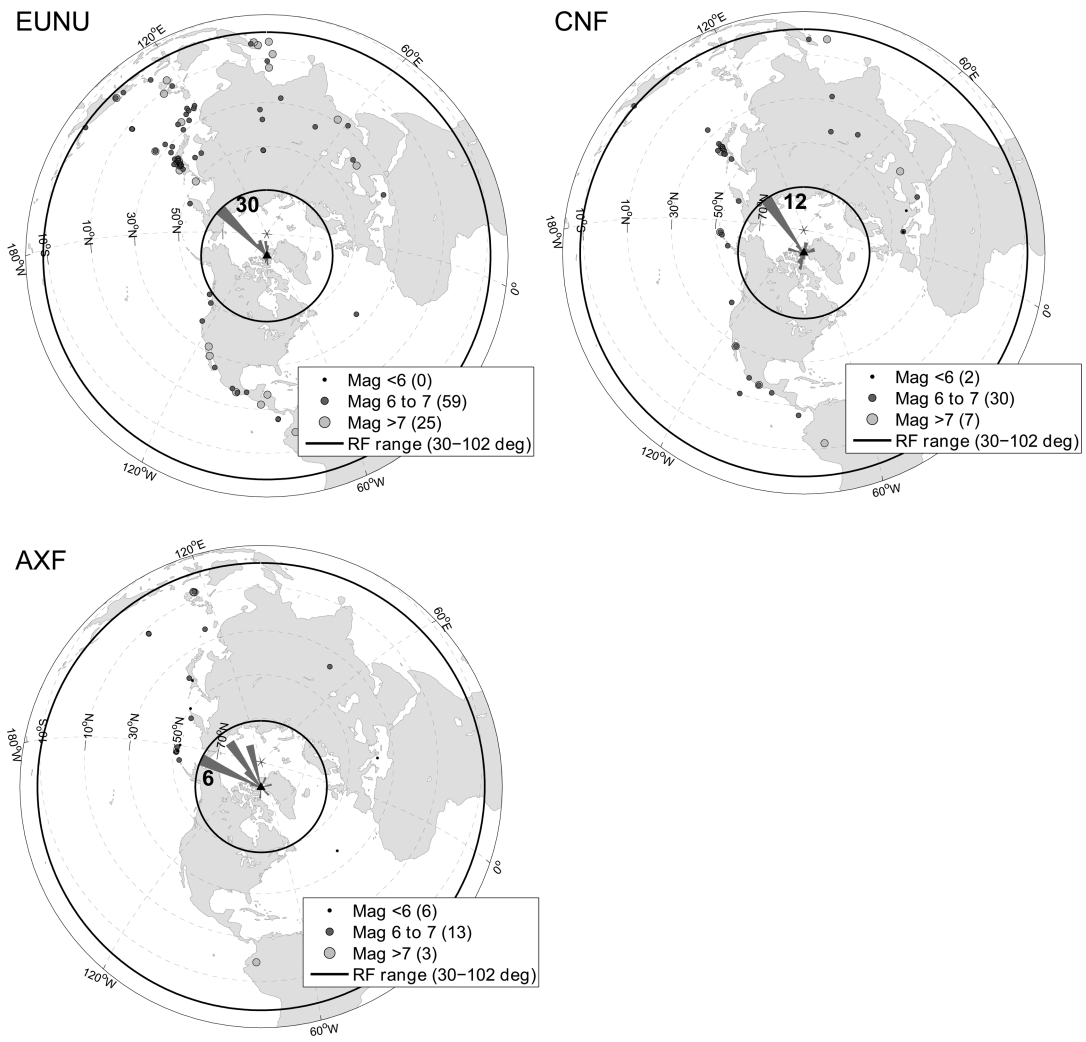

Figure 4 (*Continued*).

was removed in Q-RFs, which allowed a clearer view on the conversions only. The Z-signature was removed from the R-component by deconvolution (or L from Q) after a spectral whitening of the recorded waveforms (Clayton & Wiggins 1976). By this procedure the teleseismic wavelet, including the earthquake source effects, the instrument response and other effects on the teleseismic ray path, is focused into an impulsive waveform, thus creating a receiver function (R-RF or Q-RF) including primary and multiple conversions. During deconvolution, a Gaussian filter was applied to smooth the waveform and reduce noise. Gaussian factors of 2.5 and 3.5 were applied. Ideally, the remaining signals are dominated by the isolated *P*-to-*S* conversions in time. A normal moveout (NMO) correction accounts for theoretical differences in *Ps* conversion time with regard to the different epicentral distances between 30° and 100° (Fig. 4) of each earthquake. The NMO-corrected RFs were stacked to minimise the ambient noise and enhance the signal (Fig. 5). However, an NMO correction for *Ps* does result in a generally wrong correction of the multiple conversions, which will, consequently, not interfere coherently. It can be observed that most conversion energy is focused in the first 10–15 s after *P*-wave arrival ($t = 0$). At later delay times, the signal, for instance from crustal multiples, diminishes and cannot be distinguished from the ambient noise level ($t < 0$). After RFs were produced from all waveforms of events with magnitudes larger than 4.5, the data quality was carefully checked. First, RFs that were obviously a product of numerical errors and do not represent correct signals were deleted. These included those with amplitudes on the R-component that exceeded a threshold of 1. Once the meaningful waveforms were chosen, the data were sorted according to the root mean square of the energy from 2 to 15 s before *P*-arrival, which is regarded as a measure of the ambient noise. Different independent stacks of RFs were then assessed with successively 'noisier' waveforms containing more energy previous to the *P*-arrival. This procedure allowed a subjective determination of the maximum number of events used in the final processing. The maximum number of events was defined when the new 'noisy' RF stack showed marked differences compared to the previous stacks of events of higher quality and/or when the standard deviation of the stack increased notably. The cut-off threshold depends on the noise level at each station, the duration of deployment and, accordingly, the number of active measurements.

The principle of this procedure is illustrated in Fig. 5 where three stacks of the best third (red), the intermediate third (orange) and the noisiest third (yellow) of all RFs are shown. It can be observed that the stack of the nosiest third (yellow) is very different and has a much larger standard deviation (light grey shading) than the less noisy stacks for most of the temporary stations. In this way usually only 50–70 per cent of the events were chosen for further analysis. In contrast, the two permanent stations (ALE and EUNU) show

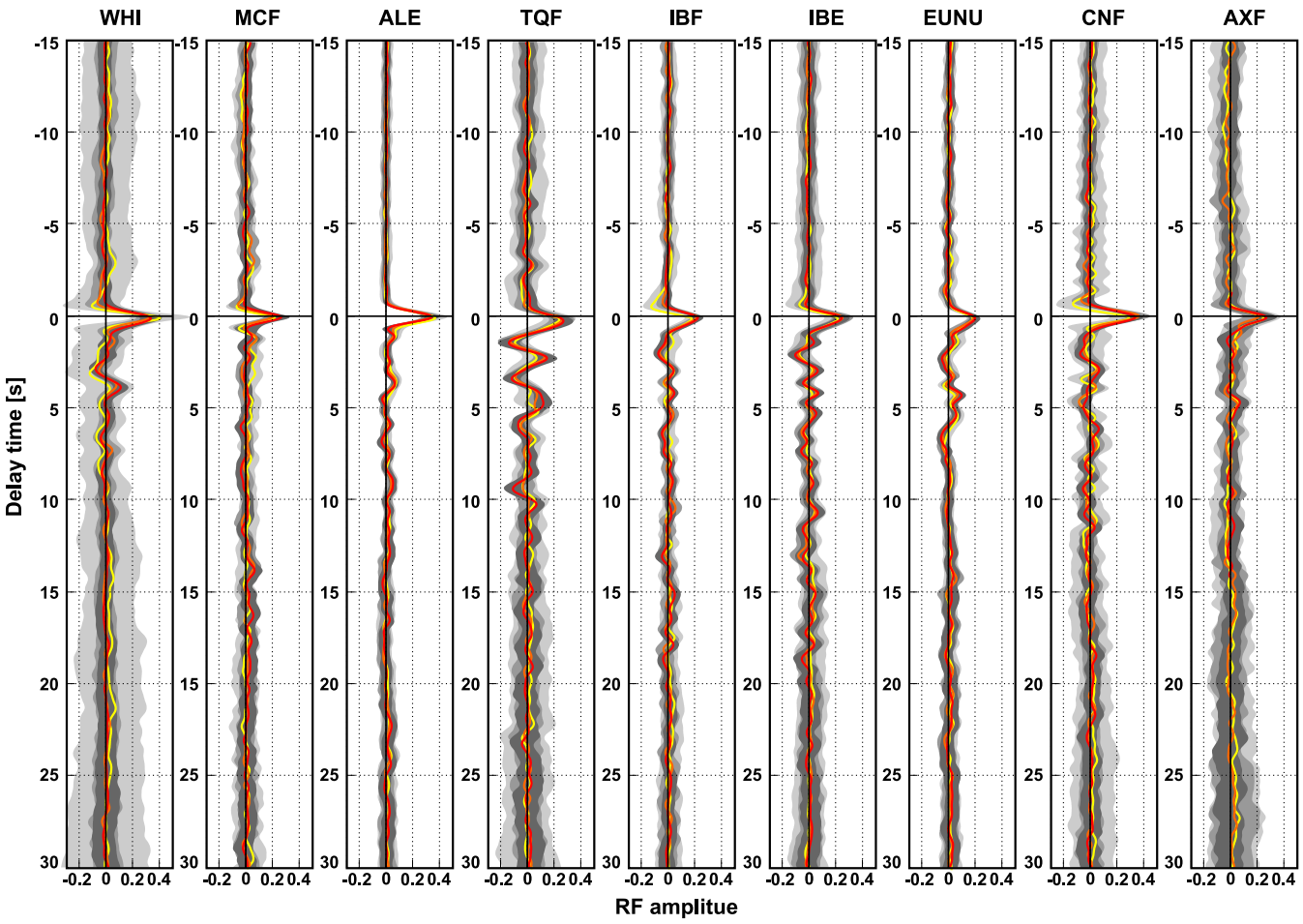

Figure 5. Variability and quality of R-receiver functions. Three independent stacks at each station are shown, sorted by the data quality (signal energy before $t = -2$ s). Red, orange and yellow show the actual stacks and grey shading the standard deviation. The best 33 per cent (red and dark grey shading), the intermediate 33 per cent (orange, middle grey shading) and the worst 33 per cent (yellow, light grey shading) of the processed and accepted receiver functions show large variability, especially for the worst stack and at temporary stations (WHI, MCF, TQF, IBF, IBE, CNF, AXF), whereas the permanent stations are very consistent (ALE and EUNU).

almost no difference between the different stacks. This is because, here, many events of similar signal strength (magnitude > 6.3) were used and, thus, signal-to-noise ratios of the single RFs do not differ significantly.

4.2 Azimuthal variations

The geology in the subsurface is likely heterogeneous for the ELLITE stations. One method to extract some of the spatial variation is the common conversion point (CCP) stacking of RFs, which places the energy of each single RF at the corresponding, theoretical conversion point in three dimensions, assuming an *a priori* velocity structure (e.g. Bostock 1998; Kosarev *et al.* 1999; Svenningsen *et al.* 2007; Schiffer *et al.* 2014). The RFs are projected along their ray paths in a 3-D model and the RF amplitude at each time step is placed at the theoretical point of conversion. The information of all RF waveforms in the 3-D volume is then projected onto a 2-D section and normalised. This imaging method exploits some of the 3-D character of the real geological structure. In the case of the ELLITE array, the conditions for the CCP stacking is not ideal since ray paths of most neighbouring stations do not cross at crustal depths for most of the stations (as shown in Fig. A1) and an entirely coherent image cannot be produced. A CCP section in comparison with the interpreted section of the ELLITE data can be found in the Appendix (Fig. A2).

Another method to extract more information is to analyse the data in separate stacks at different directions around the station. These backazimuth (BAZ) bins are chosen such that each shows a similar RF waveform, which is a good first indication that a similar geological structure underlies the station in the direction of the given bin. The BAZ bins are defined by aligning events stacked at every 10°. An example is presented in Fig. 6 where BAZ plots of both R-RFs (left) and Q-RFs (right) are shown and their corresponding total stack in the centre. The grey and white shaded background illustrates the chosen bins, which aim to group RF waveforms of similar shape. Corresponding plots for all other stations are shown in Fig. A3. Three bins in three directions were defined when data coverage was sufficient to do so. There was insufficient data coverage at MCF and AXF (the stations with the shortest live acquisition periods) to allow BAZ stacking.

Anisotropy or dipping layers in the underlying structure may add substantial complexity to the ray paths, which produce signal on the transversal RF component, caused by horizontally polarised shear waves. In general, horizontally oriented azimuthal anisotropy causes regular variations in the T-RFs of 180° periodicity, while dipping anisotropy or dipping layer boundaries produce a

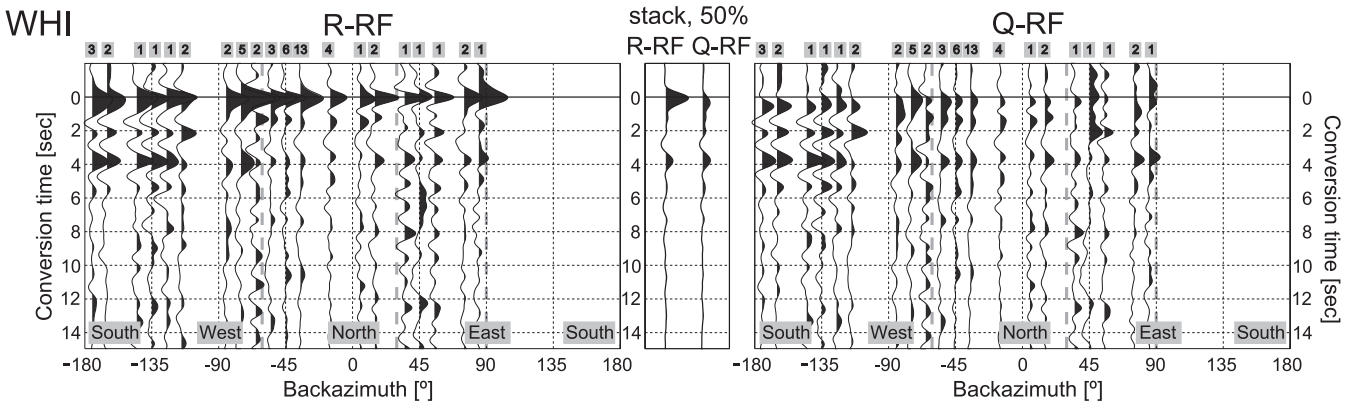

Figure 6. Backazimuth plots for station WHI with 'low frequency' ($a = 2.5$) R-RFs (left side) and Q-RFs (right). The grey shaded numbers above each trace indicate how many single RFs have been stacked for the respective backazimuth. The percentage indicates the maximum percentile (with regard to the quality of the RFs) used for the data processing, depending on the data quality at the station. In the middle, the respective stack of all events is shown. Missing stacks indicate no data coverage into the respective direction.

periodicity of 360° with the zero phase into dip direction (Frederiksen & Bostock 2000; Schulte-Pelkum & Mahan 2014). Combinations of different anisotropic fabrics and dipping layers may be arbitrarily complex (Eckhardt & Rabbel 2011). Four stations (WHI, TQF, ALE and EUNU) have shown an acceptable data quality and azimuthal coverage to investigate such features (Fig. A4). All stations show substantial and coherent signal on the T-component, which may be attributed to structural effects, instead of noise. The observed patterns seem to show a periodicity of 360°, although the azimuthal coverage is not perfect for stations WHI and TQF, indicating the presence of dipping layers or materials with a dipping anisotropy axis. Stations WHI and ALE seem to have a symmetry axis in N–S direction, while at TQF the axis might follow an SW–NE direction and W–E at station EUNU. Polarity variation can be observed down to Moho (Fig. A4, grey horizontal line) at stations WHI and TQF, and less expressed at ALE and EUNU, which might, as in the previous cases, indicate a dipping Moho interface or dipping anisotropy. A more detailed study of possible anisotropy or layer dip is beyond the scope of this paper; however, the T-RFs clearly indicate the presence of additional crustal complexity.

4.3 Apparent *S*-wave velocity ($V_{S\mathrm{app}}$)

Svenningsen & Jacobsen (2007) presented a method to extract information on the absolute shear wave velocities directly from RFs, which can be employed in inverse modelling (Schiffer *et al.* 2015). By comparing the amplitudes of the Z-RF and R-RF at $t_{Ps} = 0$ (zero delay time), which is associated with the arrival of the direct *P* wave, the apparent incidence angle ($\overline{i_p}$) can be estimated as.

$$\overline{i_p} = \arctan\left[\frac{R_{\mathrm{RF}}\left(t_{ps}=0\right)}{Z_{\mathrm{RF}}\left(t_{ps}=0\right)}\right] \tag{1}$$

For a homogeneous half-space this angle defines the *S*-wave velocity *Vs* through the equation

$$V_S = \frac{\sin\left(\frac{1}{2}\,\overline{i_p}\right)}{p} \tag{2}$$

where *p* is the wave parameter (Wiechert & Zoeppritz 1907; Nuttli & Whitmore 1961).

Svenningsen & Jacobsen (2007) showed how this principle can be used after Gaussian smoothing with successively increasing filter widths, *T*, to give apparent *S*-wave velocities, $V_{S\mathrm{app}}(T)$, sampling successively deeper velocity averages.

We apply this approach by calculating $V_{S\mathrm{app}}(T)$-curves for a range of 51 periods (T), logarithmically sampled from 1 to 10 s. The curves are calculated for each RF and the median $V_{S\mathrm{app}}$ at each sampled period T defines the $V_{S\mathrm{app}}(T)$-curve. The standard deviation is calculated from the best 68 per cent of the curves closest to the median (as proposed in Svenningsen & Jacobsen 2007).

$V_{S\mathrm{app}}$-curves were calculated for all events at each station, since the different BAZ bins may not contain a sufficient amount of high quality events. This should not be a problem as the absolute large-scale velocity structure is not expected to vary extremely between the different bins.

5 INVERSE MODELLING

Inverse modelling of RFs is a common method to extract information on the crustal and upper-mantle velocity structure (Owens *et al.* 1987; Cassidy & Ellis 1993; Sandvol *et al.* 1998a; Darbyshire 2003; Ottemöller & Midzi 2003; Schlindwein 2006). RF inversion is a non-unique problem (Ammon *et al.* 1990), mainly because of a trade-off between velocity structure and layer thicknesses for corresponding delay times and multiples that may be modelled as primary conversions. Also, RFs are sensitive to vertical *S*-wave discontinuities, whereas the *P*-wave velocity structure has less impact on delay times and amplitudes (e.g. Sandvol *et al.* 1998b; Julià *et al.* 2000; Zhu and Kanamori 2000). Joint inversion of other constraints on the absolute velocities, such as surface wave dispersion curves (Du & Foulger 1999; Julià *et al.* 2000) or the above mentioned $V_{S\mathrm{app}}$ estimates (Svenningsen & Jacobsen 2007), is a common approach to enhance the uniqueness of the inverse problem. A parametrisation of the model space in layer delay time instead of layer thicknesses (Jacobsen & Svenningsen 2008) can further stabilise the RF inversion. The two latter options were applied to the ELLITE data since dense surface wave coverage is missing.

RFs can be generally modelled as (unrotated) R-RFs (Owens *et al.* 1987; Ammon *et al.* 1990) or (rotated) Q-RFs (Kind *et al.* 1995). Both approaches are commonly used and should ideally give the same results. Inversion for both RF types was carried out in this study.

A well-established linearised, iterative least squares (LSQ) inverse method was applied (Tarantola & Valette 1982; Menke 1989;

Ammon *et al.* 1990; Jacobsen & Svenningsen 2008) to minimise a function considering data misfit, observed data uncertainty, *a priori* model uncertainty and smoothness of the model.

Formally, we define the forward mapping from model space to data space as

$$d = g(m) \tag{3}$$

where the model vector m contains velocities and thicknesses of horizontal layers, d is the data vector containing the RF and V_{Sapp} and $g(m)$ is the non-linear mapping defined by a wavefield computation and RF calculation. Then each new parameter vector (or model) m of the $k+1$st iteration is estimated by

$$m_{k+1} = m_k + \left(G^T C_d^{-1} G + B^T C_B^{-1} B + C_m^{-1}\right)^{-1} \times \left\{G^T C_d^{-1} \delta d_k + B^T C_B^{-1} \delta b_k + C_m^{-1} \delta m_k\right\} \tag{4}$$

where G is the Jacobian matrix of partial derivatives, C_d is the observed diagonal error covariance matrix, $\delta d_k = d - g(m_k)$ is the current data residual, $\delta b_k = 0 - Bm_k$ is the current model roughness and $\delta m_k = m_0 - m_k$ is the current parameter residuals relative to a preferred prior velocity stratification, m_0. The matrix B and C_B control the second-derivative roughness error of the model (Ammon *et al.* 1990; Jacobsen & Svenningsen 2008), C_m is the diagonal model covariance matrix, which includes defined *a priori* parameter covariances, σ_m^2.

5.1 Model design and forward modelling

The input data for the inverse modelling are the R-RFs and Q-RFs as well as V_{Sapp}-curves. Initially, a 1-D stratified model with layers parametrised with *S*-wave velocity (V_S), *P*-wave velocity (V_p), density (ρ) and layer thickness (Δz) is considered. This model is parametrised in layer delay time (Δt_{ps}) to enhance the stability of the RF inversion (Jacobsen & Svenningsen 2008) after the following expression (Zhu & Kanamori 2000)

$$\Delta t_{ps} = \Delta z \left(\sqrt{V_s^{-2} - p^2} - \sqrt{V_p^{-2} - p^2}\right) \tag{5}$$

where p is the usual ray parameter.

The parameter vector m used for the inversion is described by V_s and Δt_{ps} for each layer if the layer delay times are variable. In case of constant layer delay times, m only contains V_s. V_s is coupled to V_p with a fixed relationship that varies for different lithologies (Christensen 1996). Furthermore, a similar and fixed relationship is used to estimate ρ from V_p (Christensen & Mooney 1995). For each change in V_s or Δt_{ps} the layer thickness Δz must be updated after eq. (5), which is rewritten to Δz.

The data d_{mod} (RFs and V_{Sapp}) from a given parameter vector m (containing the model parameters Δt_{ps} and V_s) are calculated after eq. (3).

The synthetic RFs are calculated from the 1-D velocity models (Kennett 1983), and are convolved with the observed teleseismic wavelet (deconvolved L-component) to simulate the potentially complex teleseismic wavelet for every forward model. V_{Sapp} is calculated from the synthetic Z- and R-components.

5.2 General approach

The inverse modelling procedure was divided into two stages. The first stage utilised a minimum number of layers (usually 6–8) to infer the generalised velocity structure and major discontinuities. These results provided guiding models for the second inversion defining models with a semi-continuous stratification. The two stages were applied to every BAZ bin at every station, leading to a total of 23 BAZ bins for the ELLITE array.

Each inversion was performed individually for R-RFs and Q-RFs, each with two Gaussian filters ($a = 2.5$ and 3.5), as well as two data subsets containing a small and a large fraction of the RFs (e.g. 30 per cent and 60 per cent of the RFs) in the respective BAZ bin. These data subsets contained RFs added successively according to the quality criterion described earlier. The sizes of this fraction as well as the absolute numbers of events used are listed in Table 3. RFs of conversion times of up to 20 s were modelled. As discussed above, no clear multiple conversions are observed, partly due to the applied NMO correction to theoretical *Ps* conversion times, such that the signal energy of multiple conversions does not positively interfere and does not stand out in the ambient noise.

For each of the eight subsets (R-RF, Q-RF, $a = 2.5$, 3.5, two stacks) five inversions were performed, each with a different starting model, with velocities lying in the range $0.5\,\mathrm{km\,s^{-1}} < V_s < 4.7\,\mathrm{km\,s^{-1}}$. This resulted in a total of 40 models for each of the 23 BAZ bins. Although no major differences are seen between the resulting velocity models, the final model results were defined from the mean of the different inversion solutions.

Table 3. Station overview and processing information. The recordings at each station are subdivided into three bins (Bin1–Bin3) of different BAZ ranges, indicated by the angles. Stack 1 and stack 2 indicate the two different fractions of events that were used for the inversion and the number of events in this fraction and the standard deviation of the receiver function stack.

Station	Bins [start°/end° (number of events)]			Stack 1 [percentage, number of events, mean std]	Stack 2 [percentage, number of events, mean std]
	Bin 1	Bin 2	Bin 3		
AXF	0°/360° (22)	–	–	40, 15, 0.037	60, 22, 0.048
CNF	−90°/0° (19)	0°/90° (10)	135°/−90° (10)	35, 25, 0.038	55, 39, 0.041
EUNU	−60°/20° (49)	20°/90° (6)	90°/−120° (19)	70, 68, 0.038	85, 84, 0.040
IBE	−90°/0° (45)	0°/90° (6)	90°/−135° (7)	50, 41, 0.041	75, 58, 0.047
IBF	−90°/0° (56)	0°/90° (6)	90°/−135° (5)	66, 44, 0.037	90, 67, 0.042
TQF	−45°/45° (34)	135°/−120° (6)	−120°/−45° (24)	65, 51, 0.052	80, 64, 0.057
ALE	−40°/90° (114)	160°/−130° (26)	−110°/−40° (9)	88, 111, 0.031	98, 149, 0.032
MCF	0°/360° (23)	–	–	30, 13, 0.037	55, 23, 0.043
WHI	−60°/30° (34)	30°/90° (7)	−180°/−60° (23)	35, 36, 0.046	60, 64, 0.068

5.2.1 *Coarse crustal structure*

Each coarse model contained six layers (three sedimentary and three crustal layers), but was expanded to more layers if necessary to achieve a good initial fit (for instance, requiring velocity gradients). To be able to define the major velocity discontinuities the layer delay times Δt_{ps} were variable in this first stage. The *a priori* models at the permanent stations (ALE and EUNU) were based on published RF inverse models from Darbyshire (2003), but were simplified and reduced in layers to satisfy the model set up. The *a priori* models for the remaining temporary stations were mainly derived from crustal models in the area from RFs (Darbyshire 2003) and Moho depths from gravity modelling (Oakey & Stephenson 2008), while the intracrustal velocity structure was interpolated using additional wide angle seismic surveys (Reid & Jackson 1997; Jackson & Dahl-Jensen 2010; Funck *et al.* 2011). The *a priori* models at the temporary ELLITE stations were, accordingly, poorly constrained and, hence, were attributed large *a priori* errors for both the *S*-wave velocities of $\sigma_{Vs} = 0.6\,\mathrm{km\,s^{-1}}$ ($\sigma_{Vp} \approx 1.0\,\mathrm{km\,s^{-1}}$) and for the layer delay time. For the permanent stations where published crustal 1-D models exist, the *a priori* velocity errors were halved. In this model run, the lowermost *Vs* (the upper-mantle half-space) was kept constant at 4.6 km s^{-1} and the maximum model depth was set at 60 km.

5.2.2 *Fine crustal structure*

The final inversion of the 23 BAZ bins followed the same principle as the inversion of the coarse models described in Section 5.2.1. The crustal units were subdivided into finer layers, but the previously obtained layer boundaries were retained. Layer boundaries were introduced at 0.1, 0.3, 0.6 and 1 km depth to allow for possible sedimentary layering. 0.5 km thick layers were used from 1 to 6 km depth, and 2 km thick layers below. In this inversion, the layer delay time Δt_{ps} was fixed. Since the *a priori* parameter errors were directly adopted from the coarse inversion results, these errors were rather small. Upper-mantle discontinuities identified in the coarse models (e.g. ALE) were kept fixed and not further stratified in the fine-structure inversion modelling.

6 RESULTS AND GEOLOGICAL INTERPRETATION

RFs are most sensitive to *Vs*; however, the models are also described for *Vp*, which is coupled to *Vs* by the above mentioned *Vp*/*Vs* relation. An example for a single station result (WHI) is shown in Fig. 7. Detailed results for all other stations are shown in the Appendix (Figs A5–A12 in the Supporting Information). The grey bars in the velocity models provide an estimate of the *a posteriori* model error of the inversion approach. These are usually up to 0.15 km s^{-1} for *Vs* (0.25 km s^{-1} in *Vp*) and 2 km for the depth of the interfaces in the first inversion stage.

Distinct velocity intervals identified from the 1-D velocity models are attributed to major lithogeological layers, for example, low-velocity unconsolidated, compacted and metamorphosed sediments, medium-velocity upper and lower crystalline crust and high-velocity lowermost crust above the mantle lithosphere. There is inherent overlap of velocities for different layers such that velocity ranges cannot be defined as rigid boundaries (Christensen & Mooney 1995; Christensen 1996; Anderson 2007). This overlap leads to an uncertainty of the interpretation in addition to the already existing numerical error of the inverse modelling. It is estimated that the interpreted intracrustal lithogeological layers may have a depth uncertainty of up to 4 km. Because *Vs* is very sensitive to fracturing, whereas *Vp* is less so, an incorrectly assumed *Vp*/*Vs* ratio would bias the geological interpretation (e.g. a (meta-)sedimentary layer instead of fractured crystalline crust). High amplitude multiple conversions or multiple shallow low velocity layers would also complicate the modelling and result in an overestimation of the thickness of these layers.

Several of the models indicate large velocity gradients with very low velocities (usually $Vs < 2.2\,\mathrm{km\,s^{-1}}$ and $Vp < 4.0\,\mathrm{km\,s^{-1}}$) in the near surface. This velocity range is interpreted as representing a gradation from unconsolidated to progressively more deeply buried sedimentary rock with decreasing porosity due to compaction. Subsequent layers with $Vs \sim 2.2-2.6\,\mathrm{km\,s^{-1}}$ ($Vp \sim 4.0-4.5\,\mathrm{km\,s^{-1}}$) represent more completely lithified sedimentary successions. Layers with up to $Vs \sim 3.1\,\mathrm{km\,s^{-1}}$ ($Vp \sim 5.5\,\mathrm{km\,s^{-1}}$) are interpreted as more tightly compacted or even recrystallised, metamorphosed sedimentary successions (metasediments), although carbonate rocks are also representative of this velocity range. Higher velocities are interpreted as crystalline basement, with upper crust up to $Vs \sim 3.6\,\mathrm{km\,s^{-1}}$ ($Vp \sim 6.2\,\mathrm{km\,s^{-1}}$) and lower crust up to $Vs \sim 3.9\,\mathrm{km\,s^{-1}}$ ($Vp \sim 7.2\,\mathrm{km\,s^{-1}}$). The velocity range $Vs \sim 3.9-4.1\,\mathrm{km\,s^{-1}}$ ($Vp \sim 7.2-7.6\,\mathrm{km\,s^{-1}}$) is typical for high velocity lower crust (HVLC), attributed to magmatic intrusions or (possibly) serpentinised mantle. Upper-mantle velocities are defined with $Vs > 4.2\,\mathrm{km\,s^{-1}}$ ($Vp > 7.7\,\mathrm{km\,s^{-1}}$). The ELLITE results are described from north to south, below, followed by those for ALE and EUNU.

WHI: All models have a 1–3 km thick uppermost sedimentary layer with a large velocity gradient and similar velocities $Vs \sim 2-2.6\,\mathrm{km\,s^{-1}}$ ($Vp \sim 3-4.5\,\mathrm{km\,s^{-1}}$). The models show a metasedimentary layer to a depth of ∼7 km ($Vs \sim 3\,\mathrm{km\,s^{-1}}$, $Vp \sim 5\,\mathrm{km\,s^{-1}}$). The crustal layer to the east and southwest (Figs 7b and c) appears very uniform ($Vs \sim 3.5$, $Vp \sim 6\,\mathrm{km\,s^{-1}}$) to a depth of 26–27 km, followed by a steep gradient and a clear HVLC to Moho, which is at 40 and 43 km, respectively. In the north (Fig. 7a), the upper crust shows more variation, such as an apparent discontinuity at ∼15 km depth, but with Moho at 40 km.

MCF (Fig. A5 in the Supporting Information) does not show evidence of very low velocity sedimentary layers and starts at $Vs \sim 2.6\,\mathrm{km\,s^{-1}}$ ($Vp \sim 4.5\,\mathrm{km\,s^{-1}}$), with a smooth gradient to upper crustal velocities at ∼7–8 km depth of $Vs \sim 3.2\,\mathrm{km\,s^{-1}}$ ($Vp \sim 5.5\,\mathrm{km\,s^{-1}}$). A ∼15 km upper crustal layer ($Vs \sim 3.4-3.6\,\mathrm{km\,s^{-1}}$, $Vp \sim 6-6.5\,\mathrm{km\,s^{-1}}$) overlies a ∼20 km thick lower crustal layer ($Vs \sim 3.8-4.0\,\mathrm{km\,s^{-1}}$, $Vp \sim 6.7-7.2\,\mathrm{km\,s^{-1}}$) and a well-defined 4–5 km thick HVLC. Moho depth is at ∼42 km.

TQF (Fig. A6 in the Supporting Information) is dominated by strong sedimentary multiples that are strongest to the north and west. The 2–3 km thick sedimentary layer is characterised by very low *Vs* and *Vp* and a steep gradient from $Vs \sim 1.2-2.5\,\mathrm{km\,s^{-1}}$ in the north and west, whereas a lower velocity gradient is inferred to the south with $Vs \sim 1.8-2.5\,\mathrm{km\,s^{-1}}$. An 11–15 km thick metasedimentary layer is present in all models ($Vs \sim 2.9-3.2\,\mathrm{km\,s^{-1}}$, $Vp \sim 5-5.8\,\mathrm{km\,s^{-1}}$); however, it is thicker to the south. The crystalline crust is subdivided into a thick (10–16 km) upper crust ($Vs \sim 3.4-3.6\,\mathrm{km\,s^{-1}}$, $Vp \sim 5.9-6.5\,\mathrm{km\,s^{-1}}$), overlying a thin (5–8 km) lower crust with evidence for a 3–5 km thick HVLC to the south and west. Consistent Moho depths of 34–36 km are identified in all models.

IBF and IBE are the two stations with different instruments (Table 1), but at the same location. Despite the instrument response, which should in theory be equalised by the deconvolution, and different

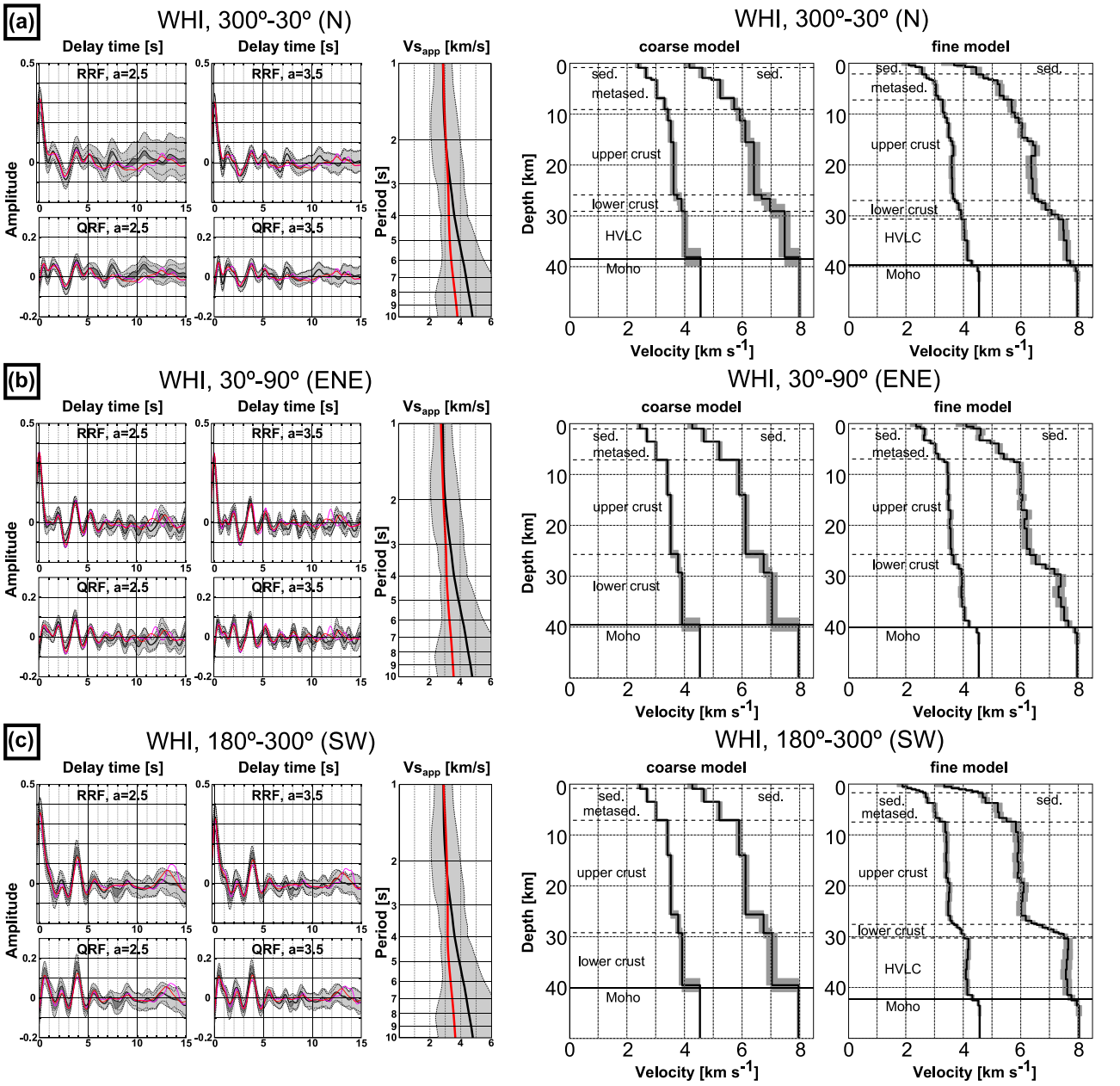

Figure 7. Inversion results of the three BAZ bins of station WHI. (a)–(c) show the different BAZ bins at this station. Left: observed (black and grey, almost coincident) and synthetic (red and magenta, almost coincident) data. The figure shows all four RF waveforms modelled (R-RF, Q-RF and $a = 2.5, 3.5$) as well as the $V_{S\mathrm{app}}$ curve. RFs: grey curves show the observed RF of stack 1; black curves show the observed RF of stack 2 (see the text and Table 3 for information on stacks). Magenta: coarse model response. Red: fine model response. Light grey shading is the envelope over the 95 per cent confidence interval of both stacks. Darker grey shading is the envelope over the two stacks. $V_{S\mathrm{app}}$: black: observed. Red: modelled. Grey: shading 68 per cent confidence interval. Right: posterior models and uncertainty.

measuring times or instrument malfunction, the same results should be expected. As mentioned in Section 3, a problem occurred with station IBF, which caused significant changes in the relative amplitudes of the vertical and horizontal components. Although these events were disregarded in the processing, the effect is still observed in other records, which suggests that other recording periods were also affected.

All models for IBE (Fig. A7 in the Supporting Information) show a well-defined 2–3 km thick low-velocity ($Vs \sim 2-3\,\mathrm{km\,s^{-1}}$, $Vp \sim 3-5\,\mathrm{km\,s^{-1}}$) sedimentary layer to the northwest and northeast; however, less well expressed to the south. The top of crystalline basement is uniformly at 17–19 km depth and overlies a ∼8–12 km thick upper crust ($Vs \sim 3.4-3.6\,\mathrm{km\,s^{-1}}$, $Vp \sim 5.9-6.4\,\mathrm{km\,s^{-1}}$) and a 10–12 km thick lower crust ($Vs \sim 3.9-4.0\,\mathrm{km\,s^{-1}}$, $Vp \sim 6.9-7.2\,\mathrm{km\,s^{-1}}$). Moho depths are shallower to the south (∼43 km) compared to the northwest and northeast (49–40 km). There are no indications of a HVLC at station IBE.

The results at IBF (Fig. A8 in the Supporting Information) are generally very similar to those of IBE. However, it was observed that the synthetic amplitudes at the 0 s conversion time were consistently overestimated by the modelling, which is a result of the variable amplitudes of the recorded horizontal and vertical

seismic components. The northeast and northwest models show similar results as the respective models at IBE, including a ∼2 km thick sedimentary layer with a steep gradient from $Vs \sim 2\,\mathrm{km\,s^{-1}}$ up to $Vs \sim 3\,\mathrm{km\,s^{-1}}$, overlying a 17–19 km thick metasedimentary layer ($Vs \sim 3.0-3.1\,\mathrm{km\,s^{-1}}$, $Vp \sim 5.0-5.5\,\mathrm{km\,s^{-1}}$), a 11 km thick upper crust ($Vs \sim 3.5-3.9\,\mathrm{km\,s^{-1}}$, $Vp \sim 5.9-6.5\,\mathrm{km\,s^{-1}}$) and a 9 km thick lower crust ($Vs \sim 4.0-4.1\,\mathrm{km\,s^{-1}}$, $Vp \sim 6.5-7.0\,\mathrm{km\,s^{-1}}$). Unlike IBE, a 3 km thin HVLC is identified in the northeast. To the south, the models agree with those of IBE down to the lower crust; however, IBF suggests a low velocity zone at the base of the crust instead of an HVLC. Because of the horizontal–vertical amplitude issues at IBF, the results from IBE are preferred because of the better data quality.

CNF (Fig. A9 in the Supporting Information) shows consistent model results for the sedimentary and crustal architecture but considerable variation in Moho depths. All models include a sedimentary layer, thickest (2–3 km) with slowest velocities ($Vs \sim 2.0-3.0\,\mathrm{km\,s^{-1}}$) to the northwest and thinnest (<1 km) with highest velocities ($Vs > 2.5\,\mathrm{km\,s^{-1}}$) to the northeast. In all models, a substantial layer of metasediments ($Vs \sim 3.0-3.2\,\mathrm{km\,s^{-1}}$, $Vp \sim 5-5.6\,\mathrm{km\,s^{-1}}$), thinnest to the northwest (∼15 km) and thickest to the northeast and south (∼20–22 km) overlies a uniform upper crust of ∼10 km ($Vs \sim 3.5-3.6\,\mathrm{km\,s^{-1}}$, $Vp \sim 6-6.5\,\mathrm{km\,s^{-1}}$) and a 12–18 km thick lower crust ($Vs \sim 3.7-4.0\,\mathrm{km\,s^{-1}}$, $Vp \sim 6.4-7.0\,\mathrm{km\,s^{-1}}$). Moho estimates vary from 47 km in the northwest, 45 km in the northeast to 48 km in the south. No evidence for HVLC is observed at CNF.

AXF: a thin (1–2 km) layer of sediments of relatively high velocity ($Vs > 2.5\,\mathrm{km\,s^{-1}}$) was inferred overlying a thin (∼3 km) metasedimentary layer ($Vs \sim 2.8-3.0\,\mathrm{km\,s^{-1}}$, $Vp \sim 4.9-5.0\,\mathrm{km\,s^{-1}}$) (Fig. A10 in the Supporting Information). The top of the crystalline basement is modelled at a depth of ∼5 km. The crust includes a ∼10 km thick upper layer ($Vs \sim 3.1-3.6\,\mathrm{km\,s^{-1}}$, $Vp \sim 5.5-6.5\,\mathrm{km\,s^{-1}}$) overlying a ∼20 km thick lower layer ($Vs \sim 3.8-3.9\,\mathrm{km\,s^{-1}}$, $Vp \sim 6.7-7.0\,\mathrm{km\,s^{-1}}$) with possible indications of a ∼3 km thin HVLC. Moho is estimated at ∼38 km depth.

ALE: RFs from the permanent station ALE resulted in considerably different models for the different azimuthal bins (Fig. A11 in the Supporting Information). To the north, there was no evidence for a sedimentary layer, whereas to the northwest and especially to the south ∼1 km thick sediments were estimated ($Vs \sim 2.0-3.0\,\mathrm{km\,s^{-1}}$, $Vp \sim 3.0-5.0\,\mathrm{km\,s^{-1}}$). Depth to inferred crystalline basement is similar in all models at ∼8 km. The upper crust ($Vs \sim 3.0-3.5\,\mathrm{km\,s^{-1}}$, $Vp \sim 5.6-6.1\,\mathrm{km\,s^{-1}}$) is ∼10 km thick to the north, ∼12 km to the south, and ∼15 km to the northwest. All models show evidence of a 5–10 km thick low velocity zone at mid-crustal depths (10–20 km). The lower crust ($Vs \sim 3.6-4.0\,\mathrm{km\,s^{-1}}$, $Vp \sim 6.2-7.1\,\mathrm{km\,s^{-1}}$) is 7–10 km thick and thickest to the north. Moho depth is estimated at ∼28 km in the north, 30 km in the south and 31 km in the northwest. All models required low upper-mantle velocities ($Vs \sim 4$ km) and an upper-mantle discontinuity with increasing depth to the north. Compared to Darbyshire's (2003) RF results, velocities in the uppermost 10 km are lower in this study and the Moho is much more weakly expressed (Fig. A11, red lines). These differences may be related to the definition of different BAZ bins (NE, SE, WNW, NNW instead of N,S, NW in this study), the usage of more events of lower magnitude by Darbyshire (2003) due to a shorter time since the installation of ALE and therefore a lower signal-to-noise ratio (1992–1999 instead of 1992–2014 in this study), the usage of a wider Gaussian filter ($a = 1.5$, instead of $a = 2.5/3.5$ in this study) or the missing additional convolution of the synthetic RF with the observed teleseismic waveform, as employed in this study (Darbyshire, personal communication, 2015). The present Moho depth estimates at ALE are 3–6 km larger than that inferred by Dahl-Jensen *et al.* (2003).

EUNU shows much less azimuthal variation than other stations (Fig. A12 in the Supporting Information). A thick sedimentary layer of 7–8 km thickness is inferred for all models but is thickest to the north where it also displays the highest velocities ($Vs \sim 3.2-4.5\,\mathrm{km\,s^{-1}}$). To the northeast and south, there are large velocity gradients ($Vs = 2-4.1\,\mathrm{km\,s^{-1}}$ and $Vs = 2.6-4.5\,\mathrm{km\,s^{-1}}$, respectively). Crystalline basement is estimated at 15–16 km depth to the north and northeast but shallower (13 km) to the south, overlying a 4–6 km thick upper crustal layer ($Vs \sim 3.5-4.0\,\mathrm{km\,s^{-1}}$, $Vp \sim 6.0-6.6\,\mathrm{km\,s^{-1}}$) and a 7–10 km thick lower crustal layer ($Vs \sim 3.6-4.1\,\mathrm{km\,s^{-1}}$, $Vp \sim 6.6-7.3\,\mathrm{km\,s^{-1}}$). Moho depths for all models are consistent at 29–31 km. Darbyshire (2003) estimated similar Moho depths but considerably higher velocities in the uppermost 10 km (Fig. A12, red lines). The differences are likely caused by the same factors as mentioned above for ALE.

7 DISCUSSION

The crustal velocity model results described in Section 6 are summarised in Figs 8–10. Fig. 8 shows the RF-based Moho depths as well crystalline crustal and (meta-)sedimentary layers compared with those derived from seismic refraction profiles in the area as well as inversion of the gravity field for Moho depth (Oakey & Stephenson 2008). Fig. 9 shows the RF-based Sverdrup Basin thickness compared to that inferred from geological and seismic reflection data. Fig. 10 shows all of the ELLITE RF results (Vp and Vs) projected along the profile shown in Fig. 2. The results presented, based on the best-fitting velocity models, are shown without error bars although they obviously do have uncertainties as discussed in Section 6.

The stations situated within the boundaries of Pearya (WHI and MCF) and the CED (IBF/IBE and CNF) show Moho at 40 km depth or more. Between both regions (TQF) and in the southernmost cratonic part of the island (AXF) Moho is calculated at ∼35 km. In the west (EUNU) and northeast (ALE) of Ellesmere Island Moho is interpreted to be very shallow at ∼30 km.

The thickness of the crystalline crust (Fig. 8b) shows significant variations across strike of the major geological boundaries. In the north (WHI and MCF) and south (AXF), crystalline crust is substantially thick (>32 km). North of the craton an 'intermediate' crystalline crustal thickness of 20–30 km can be observed (stations CNF IBE/IBF). ALE shows a similar thickness but whether this moderately thick crystalline basement is continuous to the northeast from CNF over IBF/IBE along the Vesle Fiord Thrust and the HSB to ALE is a matter of speculation. In the west (SID and southern part of North Ellesmere Domain), the crystalline crust is thinnest, 13–20 km. The general image is that the north and south are cratonic blocks (WHI, MCF, AXF) and the most central and western part of Ellesmere Island (TQF, EUNU) shows substantial crustal thinning, with a transitional zone between (CNF, IBE/IBF, ALE). Eurekan shortening has been suggested to reach as far north as the Lomonosov Ridge and the Lincoln Sea (Døssing *et al.* 2014). Although the crustal architecture indicates a cratonic origin, some of the crustal thickening at WHI and MCF could be attributed to Eurekan deformation.

The thickness of (meta-)sedimentary successions (or depth to basement, Fig. 8c) shows a different pattern. While the

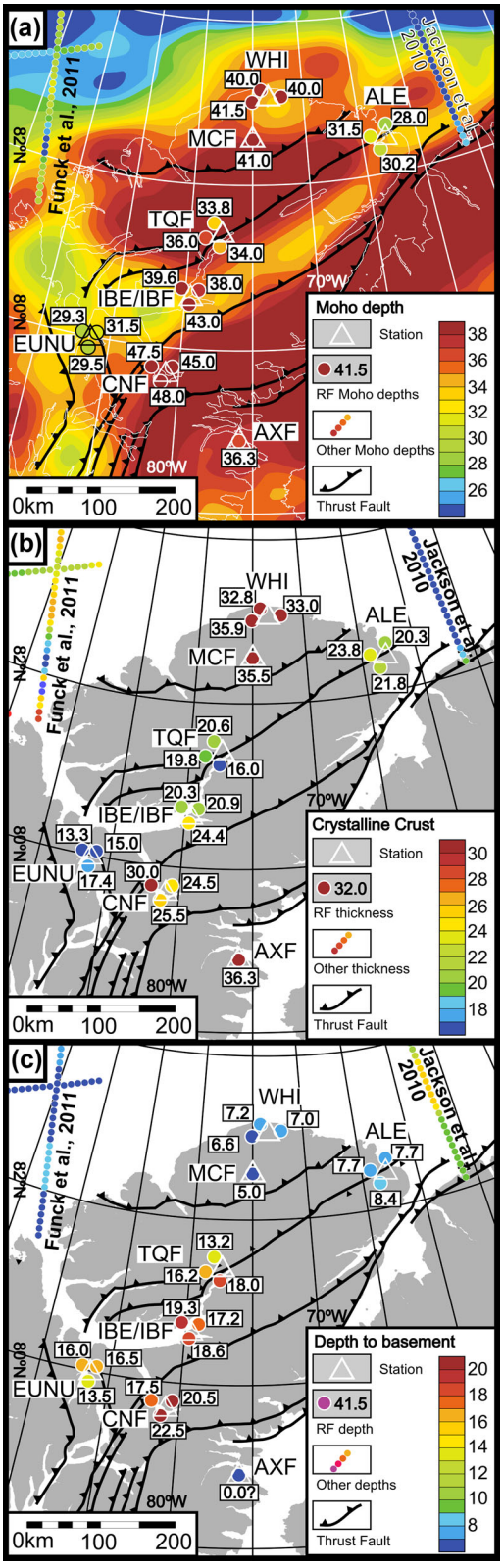

Figure 8. (a) Moho depth results from RF models (dots with values), wide angle seismic data (small dots with reference) in comparison with a gravity derived Moho map (Oakey & Stephenson 2008). The colours of all results are based on the same scale. (b) Thickness of the crystalline crust. (c) Depth to crystalline basement (combined thickness of sedimentary and metasedimentary layers).

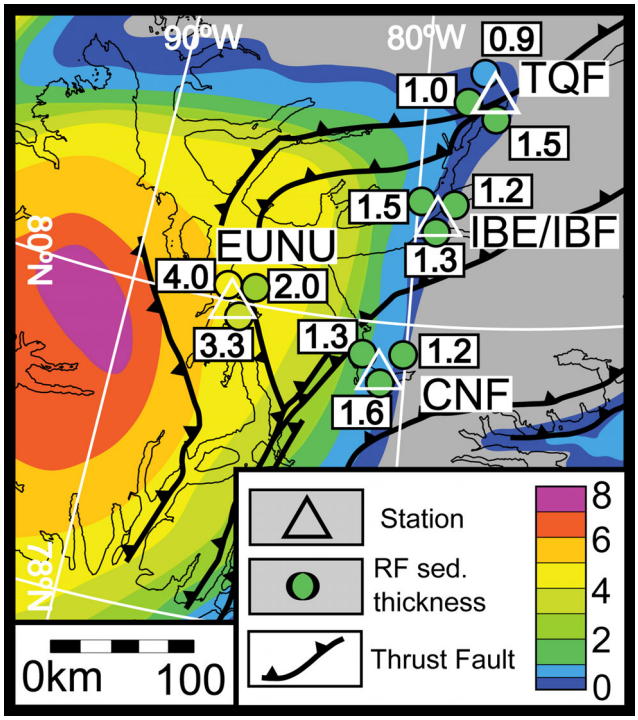

Figure 9. Estimates of the uppermost, low velocity sedimentary layer (Sverdrup Basin) from receiver functions (dots, numerical values in the white boxes in kilometres), defined by the lower boundary of the uppermost steep velocity gradient, compared with sedimentary thickness maps of the Sverdrup Basin (Embry 1990; Oakey & Stephenson 2008).

basement is shallow in the north (WHI, MCF and ALE) and south (AXF)—coinciding with the thickest basement—very thick (meta-)sedimentary successions lie atop thinned crystalline crust in the centre and to the west. The metasedimentary thickness merges with the occurrence of younger, Sverdrup Basin sediments.

Thickness estimates of the Sverdrup Basin, here defined as the uppermost steep velocity gradient representing sediment compaction, are compared with previous estimates (Embry 1991) in Fig. 9. The edges of the basin (TQF, IBE/IBF and CNF) seem to be generally thicker but slightly thinner in the centre (EUNU). The uppermost low velocity layer at AXF ($Vs \sim 2.6$ km s^{-1}, $Vp \sim 4.5$ km s^{-1}) could represent a thin layer of metasediments or heavily fractured uppermost crust, but the estimated thickness and velocities are close to resolution limits.

The section in Fig. 10 was defined to be roughly perpendicular to the major geological and topographic features of Ellesmere Island. Isovelocity lines were first interpolated laterally between the 1-D models and then vertically interpolated. In this 'profile view' different crustal domains aligned with the regional structural lineaments of the Eurekan Orogeny are illuminated. For example, thick crystalline crust with only a thin sedimentary cover in the north (Pearya; WHI and MCF) is in sharp contrast to the extremely thinned crystalline crust with very thick (meta-)sedimentary successions to the south. Pearya also shows evidence for an HVLC, perhaps indicative of lower crustal magmatic intrusions, associated with the Cretaceous HALIP lying immediately offshore (Pease *et al.* 2014).

One recently posited model regarding Pearya is that it is part of Laurentia, separated from the contiguous craton by a pericratonic backarc basin, rather than a subsequently closed oceanic basin (Hadlari *et al.* 2014). The RF-based crustal structure does display some

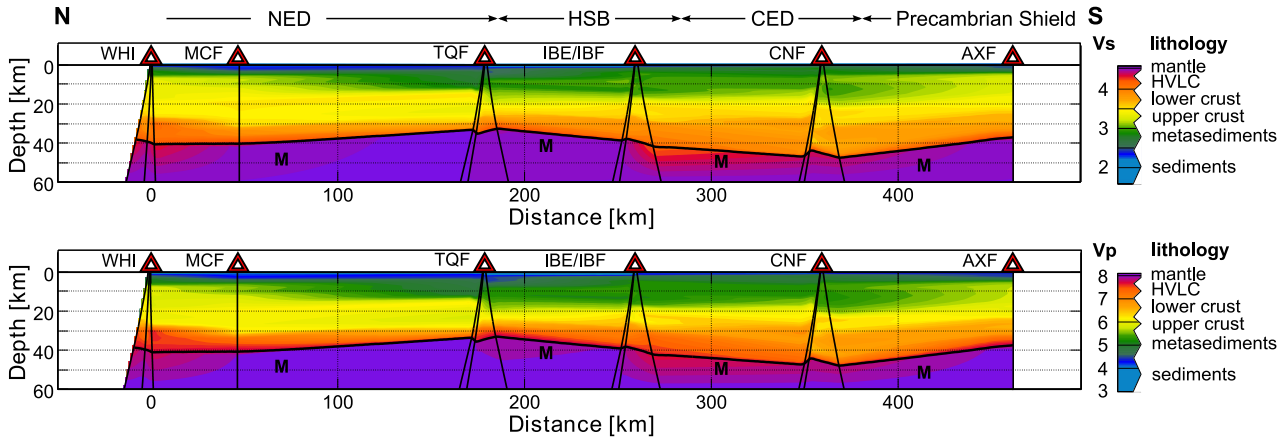

Figure 10. *S*-wave model results (middle panel) and *P*-wave model results (lower panel) interpolated between each BAZ bin and projected along the average ray path (black lines). M—Moho interpretation. White shading—interpolated areas without data coverage (∼15 km surrounding each ray path).

similarities with that of the cratonic structure inferred at AXF but is not diagnostic, particularly given the potential overprint of HALIP and Eurekan processes.

ELLITE sites immediately south of Pearya indicate a major change in crustal structure from the North Ellesmere Domain to the HSB structural domains of the Eurekan Orogeny. The layers interpreted as sedimentary and metasedimentary successions become considerably thicker, whereas the crystalline crustal layer is much thinner. Whether the transition between the two crustal domains is abrupt, gradual or more complex is not discernible given the large distance between MCF and TQF.

The RF crustal thickness results are generally compatible with gravity modelling predictions of a thicker crust underlying the North Ellesmere Domain and a thinner one under the HSB (Oakey & Stephenson 2008) and displays clear similarities with numerical models of intraplate deformation in the study area (Heron *et al.* 2015). The RF results suggest that the crust immediately adjacent to the North Ellesmere Domain–HSB boundary, as represented by the southward-vergent LHFZ (*cf.* Fig. 3) is already thin. South of station IBE/IBF, the Moho deepens gradually until it reaches a depth of 47 km in the CED (at station CNF). Deep Moho is associated with thicker crystalline crust as well as a thick metasedimentary succession. The deep Moho in this area is interpreted as downward flexure of cratonic crust beneath the Eurekan fold and thrust belt of the CED.

HVLC is present where crystalline basement appears thinnest (TQF and IBE/IBF) and these could be generically linked, either as a consequence of crustal extension and rift-related magmatism during the early formation of the Sverdrup Basin or as a result of later events.

ALE displays crystalline crustal thicknesses of 20–24 km, which is comparable to the other published estimates within the HSB. Although a thin low-velocity sedimentary layer is modelled, there is no evidence of a medium velocity metasedimentary succession. An extremely low upper-mantle velocity is inferred beneath ALE by the RFs, including a possible upper-mantle conversion of weak amplitude, dipping to the north. The expression of this structure is not well constrained and any specific interpretation very speculative. Candidates could include high mantle temperatures, a subcrustal shear zone, the transition to a different, accreted lithospheric block, the expression of a fossil subduction zone or, indeed, that this structure is an indication of very thick crust (∼48 km) rather than a discrete upper-mantle feature.

8 CONCLUSIONS

Earthquake data recorded by the temporary broad-band array ELLITE, which consisted of seven broad-band stations at six locations on a roughly NE–SW cross-section of Ellesmere Island, and at two permanent stations, Eureka and Alert on the west-central and north-eastern extremities of Ellesmere Island, respectively, have been used to compute RFs and derive velocity–depth models of the crust in an area where very little to no seismological constraints on lithosphere structure previously existed. The seismological data resulted in an image of the crustal structure of Ellesmere Island allowing regional scale tectonic interpretation. Integration with surface geology, potential field modelling and other geophysical methods will give further and more detailed insights into the tectonic evolution and links between shallow and deep structure. The results contribute important information on the crustal structure of the Canadian Arctic Archipelago and, in particular, the regional architecture of the Cenozoic intraplate Eurekan Orogen, including estimates of Moho depth and estimates of the thickness of supra- and intracrustal layers, as follows:

(1) Pearya, the northernmost structural block of Ellesmere Island, has a crustal structure that is seismologically comparable to the southernmost, cratonic, part (AXF) of Ellesmere Island. This is in sharp contrast to the crustal structure in the central part of the array, where thicker sediments and thinner crystalline crust are observed. The Mount Rawlinson Fault is a good candidate for the boundary between thinned crust of Central Ellesmere Island and the thick crust of Pearya.

(2) The seismological structure of Ellesmere Island south of Pearya represents the (late Precambrian–early Palaeozoic) Franklinian passive continental margin, deformed during the subsequent Ellesmerian and Eurekan orogenies.

(3) The North American Craton is flexed from south (AXF) to north (CNF), where it is covered by progressively thicker (meta-)sediments. Laurentian crust continues at least as far north as somewhere between CNF and IBE/IBF, close to the Vesle Fiord Thrust.

(4) The HSB comprises the thinnest crust and shallowest Moho, outside of the Sverdrup Basin.

(5) The RF estimates of the thickness of the Sverdrup Basin in central Ellesmere Island (stations TQF, IBE/IBF, CNF and EUNU) are comparable to previous estimates, but are slightly greater (by ∼1–2 km) near the edge of the basin.

(6) The observed HVLC units, both in the northernmost section (Pearya) and the central part of thinned continental crust (HSB), are most likely linked to magmatic intrusions, most likely connected to HALIP but not excluding the possibility of other magmatic events affecting the area.

ACKNOWLEDGEMENTS

The project was carried out under the umbrella of the project 'Circum Arctic Lithospheric Evolution' (CALE), which also supported some of the follow-up activities that led to the preparation of this manuscript. Funding for fieldwork was primarily derived from the Geological Survey of Canada with additional essential support from the University of Aberdeen. DeBeers Canada is thanked for financially supporting fieldwork travel in 2011 and 2012. The data processing and preparation of the manuscript were partly performed during a Ph.D. project at Aarhus University, which was part of TOPOREAL, funded by the Danish Council for Independent Research (DFF). Thanks to DFF and the participants and organisers of TOPOREAL. The authors acknowledge the support of all PCSP personnel in Resolute Bay and Ottawa, including numerous sets of Twin Otter pilots, for field support and equipment handling, TFSS personnel in Ottawa for looking after and preparing equipment and supplies and their shipment north and south, personnel at Eureka weather station for their hospitality and flexibility, Parks Canada for allowing field work to take place in Quttinirpaaq National Park, the Nunavut Research Institute in Iqaluit for their oversight and, of course, the NRCan GEM Baffin Bay Basins project, with J. Haggart of GSC Vancouver as the ELLITE project leader. M. Fowler (then GSC Calgary) is thanked for his support in getting ELLITE started in 2009–2010. J. Hunter and C. Diederik, both Resolute Bay, are thanked for their assistance and protection in the field as are S. Twelker and S. Grasby of GSC Calgary who assisted field work in 2012. C. Taylor of the University of Aberdeen designed the field observatory installations and his dedication and good company in the field in 2010 and 2011 was very much appreciated by RS. The advice and always willing assistance of A. Brisbourne (now British Antarctic Survey), D. Hawthorn and V. Lane, all SEIS-UK are also acknowledged. We are also grateful to two reviewers for very helpful and constructive comments.

REFERENCES

Alvey, A., Gaina, C., Kusznir, N.J. & Torsvik, T.H., 2008. Integrated crustal thickness mapping and plate reconstructions for the high Arctic, *Earth planet. Sci. Lett.,* **274,** 310–321.

Amante, C. & Eakins, B.W., 2009. ETOPO1 1 arc-minute global relief model: procedures, data sources and analysis, in *NOAA Technical Memorandum NESDIS NGDC-24,* doi:10.7289/V5C8276M.

Ammon, C.J., 1991. The isolation of receiver effects from teleseismic *P* waveforms, *Bull. seism. Soc. Am.,* **81,** 2504–2510.

Ammon, C.J., Randall, G.E. & Zandt, G., 1990. On the nonuniqueness of receiver function inversions, *J. geophys. Res.,* **95,** 15 303–15 318.

Anderson, D.L., 2007. *New Theory of the Earth,* Cambridge University Press.

Anfinson, O.A., Leier, A.L., Embry, A.F. & Dewing, K., 2012a. Detrital zircon geochronology and provenance of the Neoproterozoic to Late Devonian Franklinian Basin, Canadian Arctic Islands, *Geol. Soc. Am. Bull.,* **124,** 415–430.

Anfinson, O.A., Leier, A.L., Gaschnig, R., Embry, A.F. & Dewing, K., 2012b. U–Pb and Hf isotopic data from Franklinian Basin strata: insights into the nature of Crockerland and the timing of accretion, Canadian Arctic Islands, *Can. J. Earth Sci.,* **49,** 1316–1328.

Argyle, M. & Forsyth, D.A., 1994. Interpretation of data and presentation of results from the Ice Island 1986 and 1990 seismic refraction experiments. Open-File Rep., Geol. Surv. Can., **2973,** doi:10.4095/194781.

Argyle, M., Forsyth, D.A., Okulitch, A.V. & Huston, D.L., 1992. A new crustal model of the Lincoln Sea polar margin, in *Proceedings of the ICAM,* pp. 277–282, eds Thurston, D.K. & Kazuya, F., Minerals Management Service, US Department of the Interior..

Asudeh, I., Forsyth, D.A., Stephenson, R., Embry, A., Jackson, H.R. & White, D., 1989. Crustal structure of the Canadian polar margin: results of the 1985 seismic refraction survey, *Can. J. Earth Sci.,* **26,** 853–866.

Beranek, L.P., Mortensen, J.K., Lane, L.S., Allen, T.L., Fraser, T.A., Hadlari, T. & Zantvoort, W.G., 2010. Detrital zircon geochronology of the western Ellesmerian clastic wedge, northwestern Canada: insights on Arctic tectonics and the evolution of the northern Cordilleran miogeocline, *Geol. Soc. Am. Bull.,* **122,** 1899–1911.

Beranek, L.P., Pease, V., Hadlari, T. & Dewing, K., 2015. Silurian flysch successions of Ellesmere Island, Arctic Canada, and their significance to northern Caledonian palaeogeography and tectonics, *J. geol. Soc.,* **172,** 201–212.

Bostock, M.G., 1998. Mantle stratigraphy and evolution of the Slave province, *J. geophys. Res.,* **103,** 21 183–21 200.

Cassidy, J.F. & Ellis, R.M., 1993. *S* wave velocity structure of the northern cascadia subduction zone, *J. geophys. Res.,* **98,** 4407–4421.

Christensen, N.I., 1996. Poisson's ratio and crustal seismology, *J. geophys. Res.,* **101,** 3139–3156.

Christensen, N.I. & Mooney, W.D., 1995. Seismic velocity structure and composition of the continental crust: a global view, *J. geophys. Res.,* **100,** 9761–9788.

Clayton, R.W. & Wiggins, R.A., 1976. Source shape estimation and deconvolution of teleseismic bodywaves, *Geophys. J. R. astr. Soc.,* **47,** 151–177.

Coles, R.L., 1985. Magsat scalar magnetic anomalies at northern high latitudes, *J. geophys. Res.,* **90,** 2576–2582.

Dahl-Jensen, T. *et al.*, 2003. Depth to Moho in Greenland: receiver-function analysis suggests two Proterozoic blocks in Greenland, *Earth planet. Sci. Lett.,* **205,** 379–393.

Darbyshire, F.A., 2003. Crustal structure across the Canadian High Arctic region from teleseismic receiver function analysis, *Geophys. J. Int.,* **152,** 372–391.

Darbyshire, F.A., 2005. Upper mantle structure of Arctic Canada from Rayleigh wave dispersion, *Tectonophysics,* **405,** 1–23.

Davies, G.R. & Nassichuk, W.W., 1991. Carboniferous and Permian history of the Sverdrup Basin, Arctic Islands, in *Geology of the Innuitian Orogen and Arctic Platform of Canada and Greenland,* pp. 345–367, ed. Trettin, H.P., Geology of Canada 3, Geological Survey of Canada.

Døssing, A., Hopper, J.R., Olesen, A.V., Rasmussen, T.M. & Halpenny, J., 2013a. New aero-gravity results from the Arctic: linking the latest Cretaceous-early Cenozoic plate kinematics of the North Atlantic and Arctic Ocean, *Geochem. Geophys. Geosyst.,* **14,** 4044–4065.

Døssing, A., Jackson, H.R., Matzka, J., Einarsson, I., Rasmussen, T.M., Olesen, A.V. & Brozena, J.M., 2013b. On the origin of the Amerasia Basin and the High Arctic Large Igneous Province—results of new aeromagnetic data, *Earth planet. Sci. Lett.,* **363,** 219–230.

Døssing, A., Hansen, T.M., Olesen, A.V., Hopper, J.R. & Funck, T., 2014. Gravity inversion predicts the nature of the Amundsen Basin and its continental borderlands near Greenland, *Earth planet. Sci. Lett.,* **408,** 132–145.

Du, Z.J. & Foulger, G.R., 1999. The crustal structure beneath the northwest fjords, Iceland, from receiver functions and surface waves, *Geophys. J. Int.,* **139,** 419–432.

Eckhardt, C. & Rabbel, W., 2011. P-receiver functions of anisotropic continental crust: a hierarchic catalogue of crustal models and azimuthal waveform patterns, *Geophys. J. Int.,* **187,** 439–479.

Embry, A.F., 1990. Geological and geophysical evidence in support of the hypothesis of anticlockwise rotation of northern Alaska, *Mar. Geol.,* **93,** 317–329.

Embry, A.F., 1991. Mesozoic history of the Arctic Islands, in *Geology of the Innuitian Orogen and Arctic Platform of Canada and Greenland,*

pp. 371–433, ed. Trettin, H.P., Geology of Canada 3, Geological Survey of Canada.

Embry, A. & Beauchamp, B., 2008. Chapter 13 Sverdrup Basin, in *Sedimentary Basins of the World: The Sedimentary Basins of the United States and Canada,* pp. 451–471, ed. Miall, A.D., Elsevier.

Embry, A.F. & Osadetz, K.G., 1988. Stratigraphy and tectonic significance of Cretaceous volcanism in the Queen Elizabeth Islands, Canadian Arctic Archipelago, *Can. J. Earth Sci.,* **25,** 1209–1219.

Estrada, S. & Henjes-Kunst, F., 2004. Volcanism in the Canadian High Arctic related to the opening of the Arctic Ocean, *Z. Dtsch. Geol. Ges.,* **154,** 579–603.

Forsyth, D.A., Mair, J.A. & Fraser, I., 1979. Crustal structure of the central Sverdrup Basin, *Can. J. Earth Sci.,* **16,** 1581–1598.

Forsyth, D.A., Argyle, M., Okulitch, A. & Trettin, H.P., 1994. New seismic, magnetic, and gravity constraints on the crustal structure of the Lincoln Sea continent–ocean transition, *Can. J. Earth Sci.,* **31,** 905–918.

Forsyth, D.A., Asudeh, I., White, D., Jackson, R., Stephenson, R.A., Embry, A.F. & Argyle, M., 1998. Sedimentary basins and basement highs beneath the polar shelf north of Axel Heiberg and Meighen islands, *Bull. Can. Pet. Geol.,* **46,** 12–29.

Frederiksen, A.W. & Bostock, M.G., 2000. Modelling teleseismic waves in dipping anisotropic structures, *Geophys. J. Int.,* **141,** 401–412.

Funck, T., Jackson, H.R., Dehler, S.A. & Reid, I.D., 2006. A refraction seismic transect from Greenland to Ellesmere Island, Canada: the crustal structure in southern Nares Strait, *Polarforschung,* **74,** 97–112.

Funck, T., Jackson, H.R. & Shimeld, J., 2011. The crustal structure of the Alpha Ridge at the transition to the Canadian Polar Margin: results from a seismic refraction experiment, *J. geophys. Res.,* **116,** B12101, doi:10.1029/2011JB008411.

Gaina, C., Werner, S.C., Saltus, R. & Maus, S., 2011. Chapter 3 Circum-Arctic mapping project: new magnetic and gravity anomaly maps of the Arctic, *Geol. Soc. Lond. Mem.,* **35,** 39–48.

Gasser, D., 2013. The Caledonides of Greenland, Svalbard and other Arctic areas: status of research and open questions, *Geol. Soc. Lond. Spec. Publ.,* **390,** 93–129.

Gee, D.G., 2015. Caledonides of Scandinavia, Greenland, and Svalbard, in *Reference Module in Earth Systems and Environmental Sciences,* pp. 1–14, ed. Elias, S.A., Elsevier.

Grist, A.M. & Zentilli, M., 2006. Preliminary apatite fission track thermal history modelling of the Nares region of eastern Ellesmere Island and northwestern Greenland, *Polarforschung,* **73,** 113–127.

Hadlari, T., Davis, W.J. & Dewing, K., 2014. A pericratonic model for the Pearya terrane as an extension of the Franklinian margin of Laurentia, Canadian Arctic, *Geol. Soc. Am. Bull.,* **126,** 182–200.

Haines, G.V., 1985. Magsat vertical field anomalies above 40°N from spherical cap harmonic analysis, *J. geophys. Res.,* **90,** 2593–2598.

Harrison, J.C., 2006. In search of the Wegener Fault: re-evaluation of strike-slip displacements along and bordering Nares Strait by J., *Polarforschung,* **74,** 129–160.

Harrison, J.C. & de Freitas, T.A., 2007. *Geology, Agassiz Ice Cap, Ellesmere Island, Nunavut,* Geological Survey of Canada Map 2104A.

Heron, P.J., Pysklywec, R.N. & Stephenson, R., 2015. Intraplate orogenesis within accreted and scarred lithosphere: Example of the Eurekan Orogeny, Ellesmere Island, *Tectonophysics,* **664,** 202–213.

Hosseinpour, M., Müller, R.D., Williams, S.E. & Whittaker, J.M., 2013. Full-fit reconstruction of the Labrador Sea and Baffin Bay, *Solid Earth,* **4,** 461–479.

Jackson, H.R. & Dahl-Jensen, T., 2010. Sedimentary and crustal structure from the Ellesmere Island and Greenland continental shelves onto the Lomonosov Ridge, Arctic Ocean, *Geophys. J. Int.,* **182,** 11–35.

Jackson, H.R. & Reid, I., 1994. Crustal thickness variations between the Greenland and Ellesmere Island margins determined from seismic refraction, *Can. J. Earth Sci.,* **31,** 1407–1418.

Jacobsen, B.H. & Svenningsen, L., 2008. Enhanced uniqueness and linearity of receiver function inversion, *Bull. seism. Soc. Am.,* **98,** 1756–1767.

Julià, J., Ammon, C.J., Herrmann, R.B. & Correig, A.M., 2000. Joint inversion of receiver function and surface wave dispersion observations, *Geophys. J. Int.,* **143,** 99–112.

Kennett, B.L.N., 1983. *Seismic Wave Propagation in Stratified Media,* Cambridge Univ. Press.

Kind, R., Kosarev, G.L. & Petersen, N.V., 1995. Receiver functions at the stations of the German Regional Seismic Network (GRSN), *Geophys. J. Int.,* **121,** 191–202.

Kosarev, G., Kind, R., Sobolev, S.V., Yuan, X., Hanka, W. & Oreshin, S., 1999. Seismic evidence for a detached Indian lithospheric mantle beneath Tibet, *Science,* **283,** 1306–1309.

Kovacs, L.C., Srivastava, S.P. & Ruth Jackson, H., 1986. Results from an aeromagnetic investigation of the Nares Strait region, *J. Geodyn.,* **6,** 91–110.

Langston, C.A., 1979. Structure under Mount Rainier, Washington, inferred from teleseismic body waves, *J. geophys. Res.,* **84,** 4749–4762.

Lemieux, Y., Hadlari, T. & Simonetti, A., 2011. Detrital zircon geochronology and provenance of Devono-Mississippian strata in the northern Canadian Cordilleran miogeocline, *Can. J. Earth Sci.,* **48,** 515–541.

Matzka, J., 2010. A new aeromagnetic survey of the North Pole and the Arctic Ocean north of Greenland and Ellesmere Island, *Earth Planets Space,* **62,** 829–832.

Menke, W., 1989. *Geophysical Data Analysis: Discrete Inverse Theory,* Academic Press.

Neben, S., Damm, V., Brent, T. & Tessensohn, F., 2006. New multi-channel seismic reflection data from Northwater Bay, Nares Strait: indications for pull-apart tectonics, *Polarforschung,* **74,** 77–96.

Nielsen, S.B., Stephenson, R. & Thomsen, E., 2007. Dynamics of Mid-Palaeocene North Atlantic rifting linked with European intra-plate deformations, *Nature,* **450,** 1071–1074.

Nuttli, O. & Whitmore, J.D., 1961. An observational determination of the variation of the angle of incidence of *P* waves with epicentral distance, *Bull. seism. Soc. Am.,* **51,** 269–276.

Oakey, G.N. & Chalmers, J.A., 2012. A new model for the Paleogene motion of Greenland relative to North America: plate reconstructions of the Davis Strait and Nares Strait regions between Canada and Greenland, *J. geophys. Res.,* **117,** doi:10.1029/2011JB008942.

Oakey, G.N. & Damaske, D., 2006. Continuity of basement structures and dyke swarms in the Kane Basin region of central Nares Strait constrained by areomagnetic data, *Polarforschung,* **74,** 51–62.

Oakey, G.N. & Stephenson, R., 2008. Crustal structure of the Innuitian region of Arctic Canada and Greenland from gravity modelling: implications for the Palaeogene Eurekan orogen, *Geophys. J. Int.,* **173,** 1039–1063.

Oakey, G.N., Hearty, B., Forsberg, R. & Jackson, H.R., 2001. *Gravity anomaly of the innuitain region, Canadian and Greenland Arctic*. Open-File Rep., Geol. Surv. Can.

Okulitch, A.V., Dawes, P.R., Higgins, A.K., Soper, N.J. & Christie, R.L., 1990. Towards a Nares Strait solution: structural studies on southeastern Ellesmere Island and northwestern Greenland, *Mar. Geol.,* **93,** 369–384.

Okulitch, A.V. & Trettin, H.P., 1991. Late Cretaceous-Early Tertiary deformation, Arctic Islands, in *Geology of the Innuitian Orogen and Arctic Platform of Canada and Greenland,* pp. 467–485, ed. Trettin, H.P., Geology of Canada 3, Geological Survey of Canada.

Ottemöller, L. & Midzi, V., 2003. The crustal structure of Norway from inversion of teleseismic receiver functions, *J. Seismol.,* **7,** 35–48.

Owens, T.J., Taylor, S.R. & Zandt, G., 1987. Crustal structure at regional seismic test network stations determined from inversion of broadband teleseismic *P* wave forms, *Bull. seism. Soc. Am.,* **77,** 631–662.

Pease, V., Drachev, S., Stephenson, R. & Zhang, X., 2014. Arctic lithosphere—a review, *Tectonophysics,* **628,** 1–25.

Piepjohn, K., von Gosen, W., Tessensohn, F. & Saalmann, K., 2008. Ellesmerian fold-and-thrust belt (northeast Ellesmere Island, Nunavut) and its Eurekan overprint, in *Geology of Northeast Ellesmere Island Adjacent to Kane Basin and Nares Strait,* pp. 285–303, ed. Mayr, U., Nunavut, Geological Survey of Canada, Bulletin.

Reid, I. & Jackson, H.R., 1997. Crustal structure of northern Baffin Bay: seismic refraction results and tectonic implications, *J. geophys. Res.,* **102,** 523–542.

Reid, I.D., Jackson, H.R. & Tessensohn, F., 2006. The Nares 2001 geoscience project: an introduction, *Polarforschung,* **74,** 1–7.

Ricketts, B.D. & Stephenson, R.A., 1994. The demise of Sverdrup Basin: Late Cretaceous-Paleogene sequence stratigraphy and forward modeling, *J. Sediment. Res.,* **64,** 516–530.

Roest, W.R. & Srivastava, S.P., 1989. Sea-floor spreading in the Labrador Sea: a new reconstruction, *Geology,* **17,** 1000–1003.

Saltus, R.W., Miller, E.L., Gaina, C. & Brown, P.J., 2011. Chapter 4 Regional magnetic domains of the Circum-Arctic: a framework for geodynamic interpretation, *Geol. Soc. Lond. Mem.,* **35,** 49–60.

Sandvol, E., Seber, D., Barazangi, M., Vernon, F., Mellors, R. & Al-Amri, A., 1998a. Lithospheric seismic velocity discontinuities beneath the Arabian Shield, *Geophys. Res. Lett.,* **25,** 2873–2876.

Sandvol, E., Seber, D., Calvert, A. & Barazangi, M., 1998b. Grid search modeling of receiver functions: implications for crustal structure in the Middle East and North Africa, *J. geophys. Res.,* **103,** 26 899–26 917.

Schiffer, C., Balling, N., Jacobsen, B.H., Stephenson, R.A. & Nielsen, S.B., 2014. Seismological evidence for a fossil subduction zone in the East Greenland Caledonides, *Geology,* **42,** 311–314.

Schiffer, C., Jacobsen, B.H., Balling, N., Ebbing, J. & Nielsen, S.B., 2015. The East Greenland Caledonides—teleseismic signature, gravity and isostasy, *Geophys. J. Int.,* **203,** 1400–1418.

Schlindwein, V., 2006. On the use of teleseismic receiver functions for studying the crustal structure of Iceland, *Geophys. J. Int.,* **164,** 551–568.

Schulte-Pelkum, V. & Mahan, K.H., 2014. A method for mapping crustal deformation and anisotropy with receiver functions and first results from USArray, *Earth planet. Sci. Lett.,* **402,** 221–233.

Sobczak, L.W., Mayr, U. & Sweeney, J.F., 1986. Crustal section across the polar continent–ocean transition in Canada, *Can. J. Earth Sci.,* **23,** 608–621.

Srivastava, S.P., 1985. Evolution of the Eurasian Basin and its implications to the motion of Greenland along Nares Strait, *Tectonophysics,* **114,** 29–53.

Stephenson, R.A. & Ricketts, B.D., 1989. Gravity modelling in the Eurekan Orogen, Canadian Arctic Islands, in *Current Research, Part G,* pp. 225–232, Geological Survey of Canada.

Stephenson, R.A. & Ricketts, B.D., 1990. Bouguer gravity anomalies and speculations on the regional crustal structure of the Eurekan Orogen, Arctic Canada, *Mar. Geol.,* **93,** 401–420.

Stephenson, R.A., Embry, A.F., Nakiboglu, S.M. & Hastaoglu, M.A., 1987. Rift-initiated Permian to Early Cretaceous subsidence of the Sverdrup Basin, in *Sedimentary Basins and Basin-Forming Mechanisms,* pp. 213–231, eds Beaumont, C. & Tankard, A.J., Special Publication – Atlantic Geoscience Society.

Stephenson, R.A., Ricketts, B.D., Cloetingh, S.A. & Beekman, F., 1990. Lithosphere folds in the Eurekan orogen, Arctic Canada?, *Geology,* **18,** 603–606.

Stephenson, R., Oakey, G.N., Schiffer, C. & Jacobsen, B.H., 2013. Ellesmere Island Lithosphere Experiment (ELLITE): Eurekan basin inversion and mountain building, Ellesmere Island, Nunavut, *Geol. Surv. Can. Curr. Res.,* **2013-21,** 8, doi:10.4095/292859.

Svenningsen, L. & Jacobsen, B.H., 2007. Absolute S-velocity estimation from receiver functions, *Geophys. J. Int.,* **170,** 1089–1094.

Svenningsen, L., Balling, N., Jacobsen, B.H., Kind, R., Wylegalla, K. & Schweitzer, J., 2007. Crustal root beneath the highlands of southern Norway resolved by teleseismic receiver functions, *Geophys. J. Int.,* **170,** 1129–1138.

Sweeney, J.F., Balkwill, H.R., Franklin, R., Mayr, U., McGrath, P., Snow, E., Sobczak, L.W. & Wetmiller, R.J., 1986. *Transect G North American Continent-ocean Transect Program,* Geological Society of America, North America Continent-Ocean Transects Program.

Tarantola, A. & Valette, B., 1982. Generalized nonlinear inverse problems solved using the least squares criterion, *Rev. Geophys.,* **20,** 219–232.

Tegner, C., Storey, M., Holm, P.M., Thorarinsson, S.B., Zhao, X., Lo, C.-H. & Knudsen, M.F., 2011. Magmatism and Eurekan deformation in the High Arctic Large Igneous Province: 40Ar–39Ar age of Kap Washington Group volcanics, North Greenland, *Earth planet. Sci. Lett.,* **303,** 203–214.

Tessensohn, F. & Piepjohn, K., 2000. Eocene compressive deformation in Arctic Canada, North Greenland and Svalbard and its plate tectonic causes, *Polarforschung,* **68,** 121–124.

Tessensohn, F., Jackson, R.H. & Reid, I.D., 2006. The tectonic evolution of Nares Strait: implications of new data, *Polarforschung,* **74,** 191–198.

Tessensohn, F., Piepjohn, K., Estrada, S. & Damaske, D., 2012. The German Arctic research program CASE: overview, results, perspectives, *Z. Dtsch. Ges. Für Geowiss.,* **163,** 205–231.

Trettin, H.P., 1987. Pearya: a composite terrane with Caledonian affinities in northern Ellesmere Island, *Can. J. Earth Sci.,* **24,** 224–245.

Trettin, H.P., 1991. Silurian—early Carboniferous deformational phases and associated metamorphism and plutonism, Arctic Island, in *Geology of the Innuitian Orogen and Arctic Platform of Canada and Greenland,* pp. 295–341, ed. Trettin, H.P., Geology of Canada 3, Geological Survey of Canada.

Vinnik, L.P., 1977. Detection of waves converted from P to SV in the mantle, *Phys. Earth planet. Inter.,* **15,** 39–45.

Wiechert, E. & Zoeppritz, K., 1907. Über erdbebenwellen, *Nachrichten Von Ges. Wiss. Zu Gött. Math.-Phys. Kl.,* **1907,** 415–549.

Zhu, L. & Kanamori, H., 2000. Moho depth variation in southern California from teleseismic receiver functions, *J. geophys. Res.,* **105,** 2969–2980.

SUPPORTING INFORMATION

Additional Supporting Information may be found in the online version of this paper:

Figure A5. Inversion result of station MCF. Left: observed (black and grey, almost coincident) and synthetic (red and magenta, almost coincident) data. The figure shows all four RF waveforms modelled (R-RF, Q-RF and $a = 2.5, 3.5$) as well as the $V_{S\mathrm{app}}$ curve. RFs: grey curves show the observed RF of stack 1; black curves show the observed RF of stack 2 (see the text and Table 3 for information on stacks). Magenta: coarse model response. Red: fine model response. Light grey shading is the envelope over the 95 per cent confidence interval of both stacks. Darker grey shading is the envelope over the two stacks. $V_{S\mathrm{app}}$: black: observed. Red: modelled. Grey: shading 68 per cent confidence interval. Right: posterior models and uncertainty.

Figure A6. Inversion results of the three BAZ bins of station TQF. (a)–(c) show the different BAZ bins at this station. Left: observed (black and grey, almost coincident) and synthetic (red and magenta, almost coincident) data. The figure shows all four RF waveforms modelled (R-RF, Q-RF and $a = 2.5, 3.5$) as well as the $V_{S\mathrm{app}}$ curve. RFs: grey curves show the observed RF of stack 1; black curves show the observed RF of stack 2 (see the text and Table 3 for information on stacks). Magenta: coarse model response. Red: fine model response. Light grey shading is the envelope over the 95 per cent confidence interval of both stacks. Darker grey shading is the envelope over the two stacks. $V_{S\mathrm{app}}$: black: observed. Red: modelled. Grey: shading 68 per cent confidence interval. Right: posterior models and uncertainty.

Figure A7. Inversion results of the three BAZ bins of station IBE. For details see Fig. A5.

Figure A8. Inversion results of the three BAZ bins of station IBF. For details see Fig. A5.

Figure A9. Inversion results of the three BAZ bins of station CNF. For details see Fig. A5.

Figure A10. Inversion results of station AXF. For details see Fig. A5.

Figure A11. Inversion results of the three BAZ bins of station ALE. The red velocity models show results from Darbyshire (2003) into similar directions. For details see Fig. A5.

Figure A12. Inversion results of the three BAZ bins of station EUNU. The red velocity models show results from Darbyshire (2003) into similar directions. For other details see Fig. A5. (http://gji.oxfordjournals.org/lookup/suppl/doi:10.1093/gji/ggv539/-/DC1).

APPENDIX

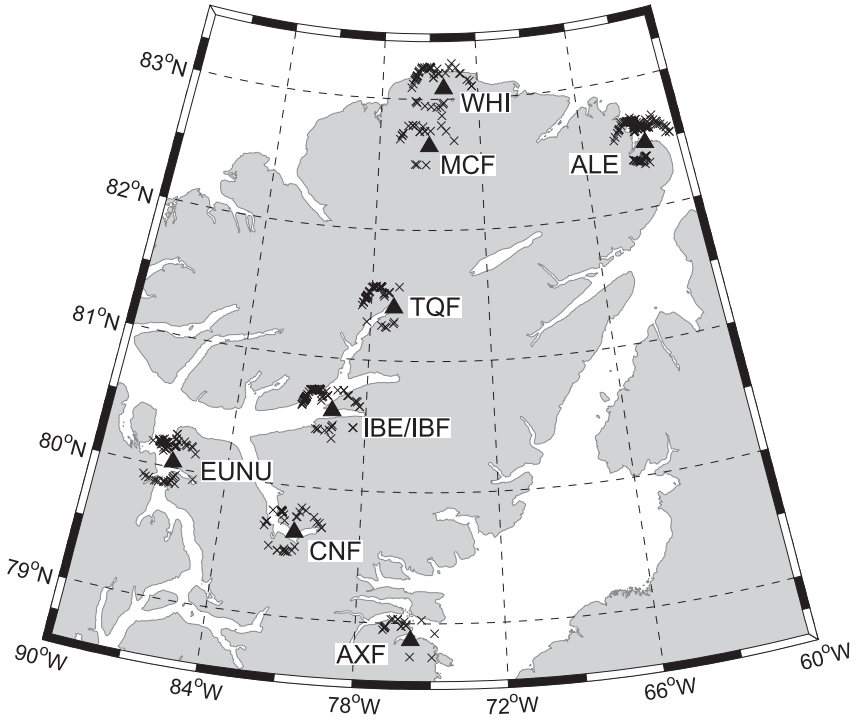

Figure A1. Map of the seismometers used (black triangles) and the 'piercing points' (crosses), where the theoretical ray path of each event at each station cross-cuts the base of a homogeneous, 1-D crustal layer of 40 km thickness and $Vp = 6.4$ km s^{-1} and $Vs = 3.7$ km s^{-1}.

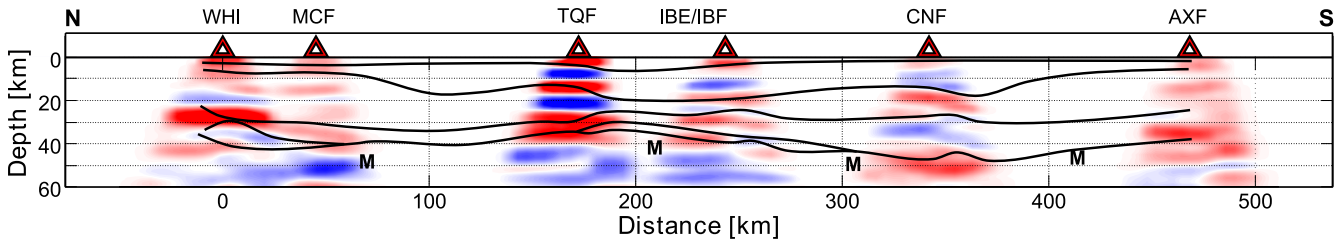

Figure A2. CCP stack of the receiver functions of ELLITE. Red indicates a downward velocity increase. Blue indicates a downward velocity decrease. Multiples must be especially considered which can have both polarities. In particular multiples originating from sedimentary basins can cause strong multiple phases down to Moho (e.g. at station TQF). Black lines represent lithological boundaries from structural interpretation of Fig. 10.

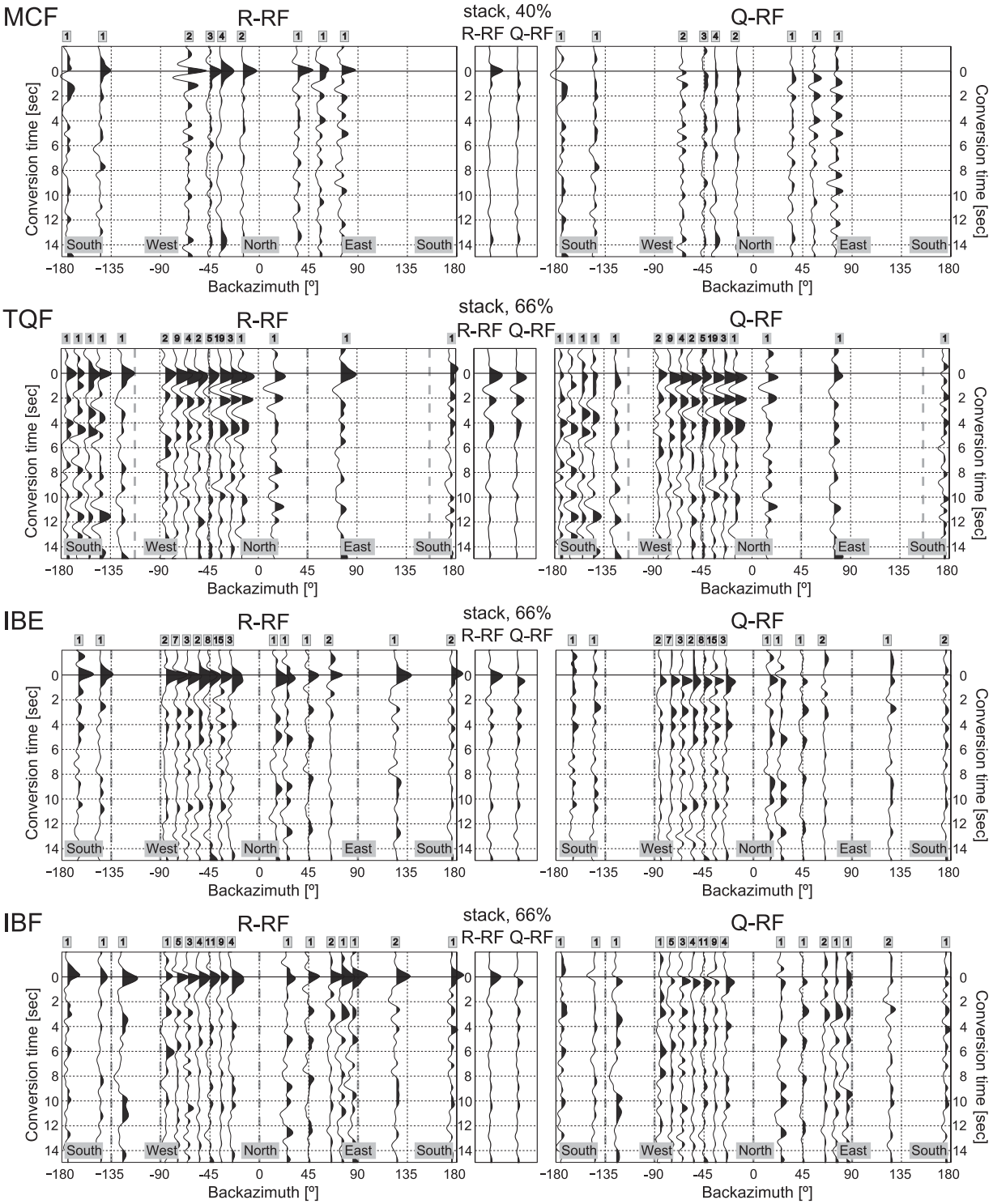

Figure A3. Backazimuth plots for all stations (except WHI, which can be seen in Fig. 6) with 'low frequency' ($a = 2.5$) R-RFs (left side) and Q-RFs (right). The grey shaded numbers above the single traced indicate how many single RFs have been stacked for the respective backazimuth range. The percentage indicates the maximum percentile (with regard to the quality of the RFs) used for the data processing, depending on the data quality at the station. In the middle the respective stack of all events is shown. Missing stacks indicate no data coverage in the respective direction.

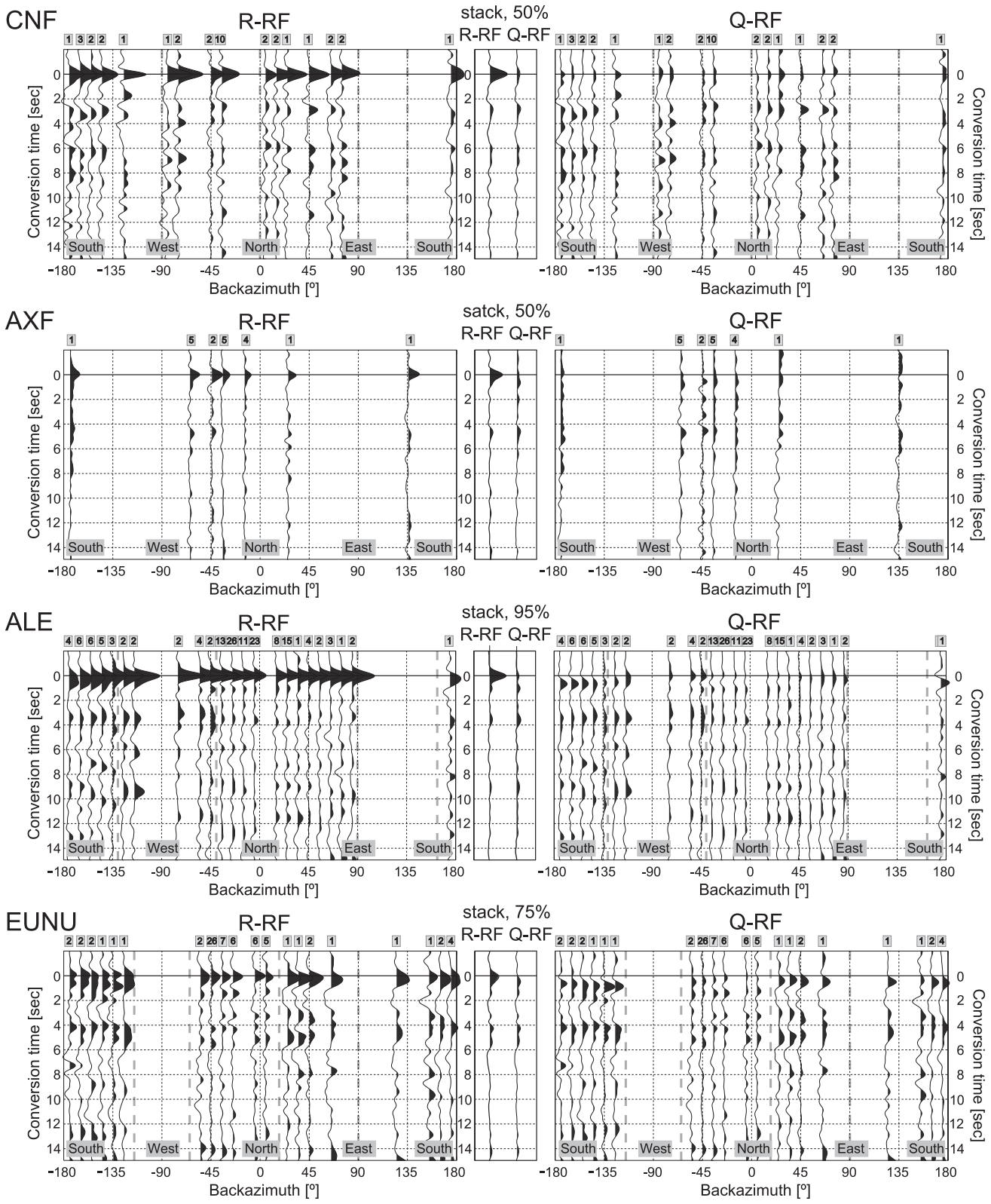

Figure A3 (*Continued*).

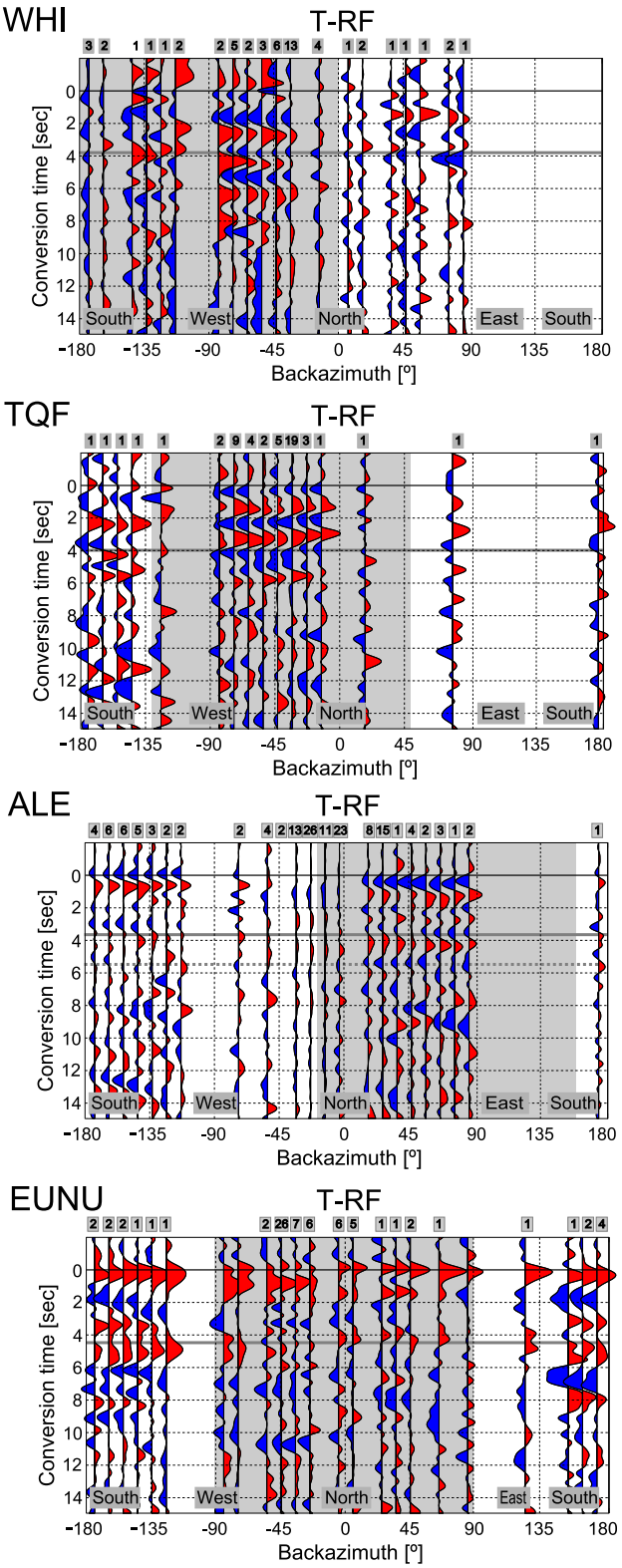

Figure A4. Backazimuth plots for stations WHI, TQF, ALE and EUNU with 'low frequency' ($a = 2.5$) T-RFs (left side). The grey shaded numbers above the single traced indicate the number of stacked RFs for the respective backazimuth range. The grey shaded areas indicate the interpreted backazimuth ranges with of the same RF phases (negative or positive) and the boundary, accordingly, the symmetry axis of the underlying structure.